An Online Monitoring and Fault Location Methodology

for Underground Power Cables

by

Sudarshan Govindarajan

A Thesis Presented in Partial Fulfillment
of the Requirements for the Degree
Master of Science

Approved March 2016 by the
Graduate Supervisory Committee

Keith E. Holbert, Chair
Gerald Heydt
George G. Karady

ARIZONA STATE UNIVERSITY

May 2016

ABSTRACT

With the growing importance of underground power systems and the need for greater reliability of the power supply, cable monitoring and accurate fault location detection has become an increasingly important issue. The presence of inherent random fluctuations in power system signals can be used to extract valuable information about the condition of system equipment. One such component is the power cable, which is the primary focus of this research.

This thesis investigates a unique methodology that allows online monitoring of an underground power cable. The methodology analyzes conventional power signals in the frequency domain to monitor the condition of a power cable.

First, the proposed approach is analyzed theoretically with the help of mathematical computations. Frequency domain analysis techniques are then used to compute the power spectral density (PSD) of the system signals. The importance of inherent noise in the system, a key requirement of this methodology, is also explained. The behavior of resonant frequencies, which are unique to every system, are then analyzed under different system conditions with the help of mathematical expressions.

Another important aspect of this methodology is its ability to accurately estimate cable fault location. The process is online and hence does not require the system to be disconnected from the grid. A single line to ground fault case is considered and the trend followed by the resonant frequencies for different fault positions is observed.

The approach is initially explained using theoretical calculations followed by simulations in MATLAB/Simulink. The validity of this technique is proved by comparing the results obtained from theory and simulation to actual measurement data.

To,

Lakshmi and T. D. Govindarajan,

Vanaja and Dr. Venketa Parthasarathy.

ACKNOWLEDGMENTS

I would like to express my sincere appreciation and gratitude to my advisor, Dr. Keith E. Holbert, for giving me the opportunity to work on this project. He has always been a great source of encouragement and motivation. I appreciate his dedication and patience in assisting me throughout the term of my graduate degree.

I would like to thank Dr. Gerald Heydt and Dr. George G. Karady for being a part of my graduate supervisory committee.

Mr. Young Deug-Kim, my colleague, provided useful insights and assistance towards the development of this project. I would like to acknowledge his contribution for providing me with actual system data for this project.

I would also like to thank my friends for their support and for being a part of my graduate experience.

I express my sincere gratitude to my aunt and uncle, Vanaja and Dr. Venketa Parthasarathy. Thank you for your unwavering support and belief.

Finally, I would like to thank my parents, Lakshmi and T. D. Govindarajan. I am grateful to them for their endless love, encouragement and moral support through thick and thin.

TABLE OF CONTENTS

Page

CHAPTER Page

CHAPTER Page

LIST OF TABLES

Table Page

LIST OF FIGURES

Figure Page

Figure Page

LIST OF SYMBOLS

α	Attenuation Constant
β	Phase Shift
D	Distance between Phases
d_c	Distance between Conductors
d	Per Unit Distance to Fault Point
d_{bund}	Distance between Bundles
e_r	Dielectric Constant
E_i	Incident Signal Voltage
E_r	Reflected Signal Voltage
ε_0	Vacuum Permittivity
ε_{se}	Relative Permittivity of Insulation between Sheath and Earth
fr_{nC}	n^{th} Resonant Frequency in Cable Power System
fr_{nCF}	n^{th} New Resonant Frequency in Faulted Cable Power System
fr_{nT}	n^{th} Resonant Frequency in TR Connected Cable Power System
f_{st}	Standing Wave Frequency
Δf	Frequency Step Size, Frequency Resolution
GMD	Conductor Geometrical Mean Distance
GMR	Conductor Geometric Mean Radius
g	Gravitational Acceleration
γ	Propagation Constant
H_C	Transfer Function for Cable Power System

H_T	Transfer Function for Transformer Connected Cable Power System
H_{CF}	Transfer Function for Faulted Cable Power System
I_0	Zero-sequence Current
I_R	Current at Load Side
I_S	Current at Source Side
I_{pre}	Pre-fault Current
I_{sup}	Superposition Current
k_p	Proximity Effect Factor
k_s	Skin Effect Factor
L_{max}	Maximal Cable Length
L_{min}	Accuracy of Distance Measurement
l	Cable Length
n	Data Point
npts	Number of Data Points per Window
R_{75}	Resistance at 75°C
R_{AC}	Equivalent Resistance in AC Circuit Condition
R_{DC}	Equivalent Resistance in DC Circuit Condition
R_F	Fault Resistance
r	Outer Radius of Core Conductor
r_0	Conductor Radius, Cable Radius
r_{bund}	Equivalent Radius of the Conductor
$r_{s,out}$	Sheath Outer Radius

r_{xn}	Cross-correlation between Discrete Incident Signal and Noise
r_{xx}	Autocorrelation of the Discrete Incident Signal
r_{xy}	Cross-correlation
ρ	Reflection Coefficient
σ^2	Signal Variance
τ	Time Delay, Translation in Time-Frequency Analysis
Δt	Sampling Interval or Sampling Time Interval
t	Time
t_d	Time Difference between t_A and t_B
T	Angle between Zero-sequence Current and Fault Current
$tan\ \delta$	Dissipation Factor
τ_p	Surge Propagation Time
μ_0	Vacuum Permeability
μ_k	Propagation Parameter
V_S	Voltage at Source Side
V_R	Voltage at Load Side
v_c	Speed of Light
v_p	Propagation Velocity, Wave Speed
ω	Angular Frequency
X_m	Cable Reactance
$x(t)$	Random Time Signal
y	Constant ($y = 1$ for 1, 2, 3 Core Cables, y=1.5 for Pipe-Type Cables)

Z_{0m}	Zero-sequence Cable Impedance
Z_{1m}	Positive-sequence Cable Impedance
Z_F	Impedance at the Discontinuity
Z_c	Characteristic Impedance
Z_{in}	Equivalent Impedance
Z_m	Cable Impedance
$\otimes$	Convolution
$\delta(\tau)$	Unit Impulse Sequence

LIST OF ABBREVIATIONS

ANN	Artificial Neural Networks
AWG	Arbitrary Waveform Generator
CT	Current Transformer
DFT	Discrete Fourier Transform
DSP	Digital Signal Processing
FDR	Frequency Domain Reflectometry
FFT	Fast Fourier Transform
HFCT	High Frequency Current Transformer
IEEE	Institute of Electrical and Electronics Engineers
PD	Partial Discharge
PSD	Power Spectral Density
TDR	Time Domain Reflectometry
THD	Total Harmonic Distortion
TFDR	Time Frequency Domain Reflectometry
VLF	Very Low Frequency

CHAPTER 1

INTRODUCTION

Underground power cables represent an important part of the power system. Recent years have witnessed an increase in the reliability and efficiency of underground power systems making them a good alternative to overhead lines for transmitting power in specific cases.

The vulnerability of power cables to failures due to aging or defects occurring over time has encouraged researchers to study and develop cable diagnostic and monitoring systems [1]. It has been reported that more than half of the cable failures occur due to electrical reasons [2]. Existing technologies for cable monitoring and diagnosis are based on evaluating partial discharge, dissipation factor (tan δ), withstand voltage, DC leakage current, recovery voltage or polarization/depolarization current [3]. Most of these methods are based on offline testing conditions, and require specific instrumentation and highly experienced technicians. Even though some online partial discharge monitoring systems have been commercialized, they still suffer from the limitation of not measuring signals of small magnitude (i.e., microvolt range) and noise interference [4].

Although being underground has its own advantages, identification of cable fault location is an important aspect pertaining to underground cables since they are not easily accessible. Effective cable diagnosis and accurate identification of fault location would ensure greater reliability of underground power systems and faster restoration of power in the network in case of contingencies.

To overcome the above drawback, improved methodologies for detection of cable fault location have been developed. These methods are mainly based on time domain

analysis of fault voltage and current signals, signal arrival time calculation, infrared imaging, time domain reflectometry and a variety of high frequency characteristics [5]. Fault location identification based on the analysis of travelling wave natural frequency is one good example [6] [7] [8]. However, these approaches are still under study and have not been developed for real time testing.

Owing to the shortcomings in existing methodologies, recent literature has focused on frequency domain signal analyses for identifying anomalous conditions occurring in underground cable systems. These approaches are believed to yield high accuracy without the need for additional instrumentation and are passive, i.e., they do not require disconnection from the power grid [9] [10] [11].

This thesis focuses on evaluating the feasibility of a new proposed methodology which is based on analyzing conventional power signals using frequency domain analysis techniques. The behavior of resonant frequencies observed in the system in the presence of inherent signal fluctuations is a key aspect of this methodology. These resonant frequencies are directly related to the cable parameters and are unique to each cable. The characteristics of the cable material, layout and changes in internal impedance, such as due to fault conditions and aging of cable material are other factors that influence the resonant frequencies.

Chapter 2 identifies and explains the existing techniques that are presently used for underground power cable diagnosis and monitoring. Since cable fault detection is also an important aspect of the proposed methodology, existing methods, both online and offline, for cable fault detection are also discussed. The shortcomings of these techniques are

mentioned and key aspects which distinguishes the proposed methodology from existing techniques are discussed.

Chapter 3 provides a detailed description of the proposed methodology. Analytical expressions for the system under consideration are presented, followed by frequency domain analysis of system signals. This chapter focuses primarily on the behavior of the system resonant frequency. A theoretical background of the transmission system model is reviewed. Expressions for the system transfer function are obtained for two cases: a simplistic case which models only the cable system and a realistic case which models a transformer-connected cable power system. Frequency domain analysis is carried out by computing the power spectral density (PSD) of the system signals. The importance of inherent noise in the system is explained by examining the PSD plots.

Chapter 4 focuses on simulating the system and comparing the results with theoretical studies on the resonant frequency behavior discussed in Chapter 3. Frequency domain analysis of the system is carried out by performing computer simulations in MATLAB/Simulink. The behavior of resonant frequencies is studied under fault conditions simulated at different positions along the cable. This chapter also shows the effect of the transformer on the resonant frequency and justifies the effectiveness of window functions for obtaining distinct resonant frequencies.

Chapter 5 validates the simulation results with real system data. The measurement point of the real data and the percentage of noise in the system are estimated by comparing the PSDs of the simulated and real systems. Finally, Chapter 6 summarizes the work carried out, presents conclusions and proposes future works.

CHAPTER 2

EXISTING METHODOLOGIES FOR POWER CABLE MONITORING AND FAULT LOCATION IDENTIFICATION

With the growing demand for undergrounding of electric lines, the topic of power cable diagnostics and fault location identification has attracted a lot of attention in recent years. This chapter discusses the dissipation factor (tan δ) test and partial discharge test, two widely used cable diagnosis techniques today. Cable fault location methods are reviewed under two main categories, namely online and offline methods. The theoretical concept and limitations of each of the above mentioned methods are discussed.

2.1 Cable Diagnostic and Monitoring Techniques

Effective cable diagnosis ensures reliability and consistency in the delivery of electricity. Accurate measurement of cable defects and detection of cable faults can reduce the failure rate of power cables. Some of the commonly used cable diagnostic techniques for detecting cable defects are partial discharge, dissipation factor (tan δ), withstand voltage, DC leakage current, polarization / depolarization current and recovery voltage [12].

2.1.1 Dissipation Factor (tan δ) Test

The tan δ test, also termed as loss angle or dissipation factor test, is a method to diagnose insulation defects in a power cable. This is mainly carried out to predict the life of cable insulation to plan ahead for cable replacement. Some common cable insulation defects are water trees, electrical trees, moisture and air pockets to name a few. The tan δ test can also serve as a means to determine what other tests may be worthwhile to monitor cable condition.

The principle of the tan δ test is based on the concept of an ideal capacitor. For the case of an ideal capacitor, the voltage and current are 90 degrees apart in phase and the current flowing through the insulator is capacitive. The presence of impurities in cable insulation provides a conductive path for the flow of current and introduces a resistive component to the current flowing. Under such conditions, the phase difference between the voltage and current is no longer 90 degrees. The extent to which the phase difference is less than 90 degrees is an indication of the quality of insulation. For a good insulator, the resistive component of the current should be low which corresponds to less defects in cable insulation. Fig. 2.1 shows the test setup and a vector representation of this effect.

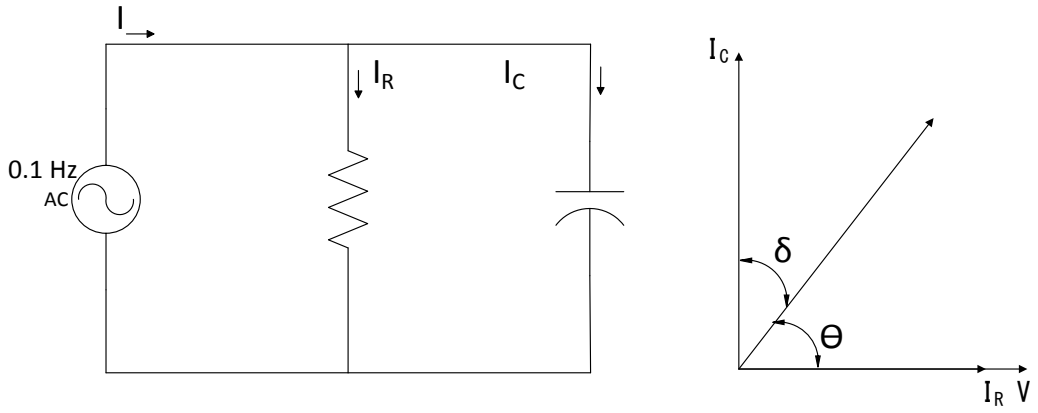

Fig. 2.1 Equivalent Circuit for tan δ Test and Vector Diagram [13].

The tan δ testing method can also be applied to transformer windings and bushings in addition to cable insulation. In order to carry out this test, the component to be tested must be isolated from the system. This implies that it involves offline testing which is a drawback of this method. A very low frequency (VLF) test voltage is applied to the cable and the tan δ controller takes the measurements. The very low frequency

range is typically between 0.01 Hz and 0.1 Hz. The applied test voltage magnitude is initially set at the normal line to neutral voltage. If the value of tan δ is within the acceptable range and indicates good cable insulation, the test voltage is raised to up to 2 times the operating voltage. The results for the two different voltage levels are compared and an analysis is made. This test takes around 15-20 minutes, depending on the instrument settings and voltage levels used.

Now, there are a couple of reasons as to why a very low frequency voltage is applied. First, it is practically infeasible to test a cable that is several kilometers long with a 60 Hz power supply. Low frequency testing also involves significantly less power compared to testing at 60 Hz. Second, the dissipation factor (tan δ) can be expressed as follows:

$$\text{Dissipation factor } (\tan\delta) = \frac{I_R}{|I_C|} = \frac{V/R}{V\,2\pi fC} = \frac{1}{2\pi fCR} \qquad (2.1)$$

From (2.1), tan δ is inversely proportional to the frequency. Therefore, at low frequencies, the value of tan δ is high which makes it easier to measure.

The results of the test are interpreted based on the plot of tan δ vs. voltage. If the cable insulation is in good condition, the change in the tan δ value for different voltage levels will be small. However, if there is significant variation in the loss factor for different voltage levels, it indicates failing insulation.

This test can typically be applied to cables with length ranging from 3 to 5 miles. However, cables upto 30 miles long can also be tested. It is preferred to keep the length of the cable section under test as short as possible for highly precise results.

The main drawback of this method is that it involves offline testing, i.e., the cable has to be disconnected from the power system. Also, the tan δ test cannot be used to determine the location of cable defects. This method assesses the condition of insulation between two points on a cable. It cannot distinguish between a minor or major defect but gives an overall general idea of the condition of cable insulation.

2.1.2 Partial Discharge Testing

Partial discharge (PD) is a result of electrical stress in the insulation or insulation surface usually accompanied with the emission of sound, heat or chemical reactions. Partial discharges are electrical sparks of small magnitude that occur within medium and high voltage cable insulation. This leads to deterioration of insulation, and eventually insulation failure. Surface discharge, electrical trees, cavities and voids are some partial discharge causing defects.

Partial discharge testing can be applied to cables, power transformers and bushings, switchgears and generators. Data obtained from a partial discharge test can provide important information about the quality of insulation. Partial discharge activity can be monitored over time and decisions regarding the repair or replacement of equipment can be strategically made. Partial discharge testing can be classified into two types, offline testing and online testing.

Offline testing has the capability to estimate the exact location of the defect on relatively aged equipment. This helps in maintenance planning or replacement of the cable depending on the severity of the defect. The drawback of offline testing, as mentioned earlier, is that the equipment must be disconnected from the grid.

A typical 50/60 Hz offline partial discharge test setup will first require the cable under test to be disconnected from the system. A series of tests are then carried out on the cable. The first test is a sensitivity assessment test. The aim of this test is to determine the smallest detectable PD signal (picoCoulomb (pC) range) under test conditions [14]. The test setup is shown in Fig. 2.2.

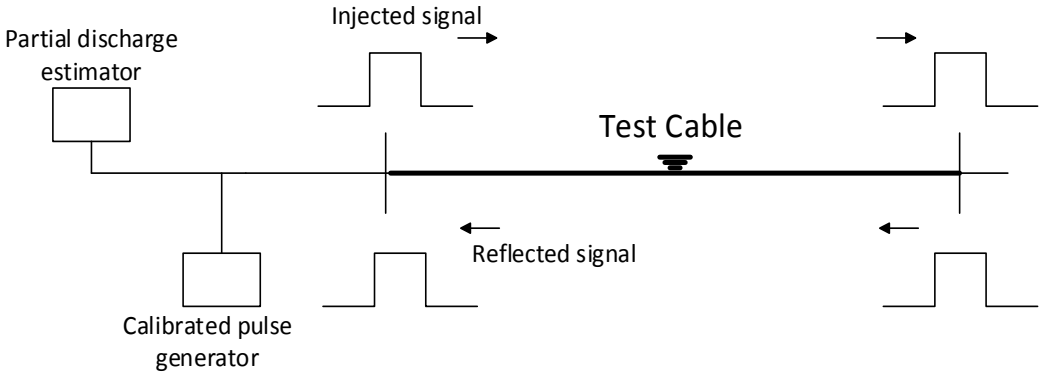

Fig. 2.2 Setup to Assess the Threshold of Sensitivity during a Field Test [14].

Next, a PD magnitude calibration test is carried out. The aim of this test is to calibrate the instrument for measuring the charge generated during partial discharge. This is done by injecting a large signal at one end of the cable and recording it at the far end. This signal is then evaluated by integrating it with respect to time.

The next step involves PD testing under voltage stress conditions. Initially, the voltage is ramped up quickly to its operating level (1 p.u.) and kept at this level for a few minutes. It is then ramped to a maximum of around 2 p.u. and then brought down to zero as fast as possible. A series of data sets are recorded during this stress cycle. The rise and fall in voltage levels determines the PD inception voltage (PDIV) and the PD extinction voltage (PDEV). The final step involves data analysis, reporting and matching the estimated PD to its actual physical location along the underground cable [14].

Online partial discharge testing is conducted during real operating conditions. This includes typical temperatures, voltage stresses and vibration levels. It does not involve overvoltage conditions that can adversely affect the cable, hence it is a non-destructive testing method. Online PD testing is more economical compared to offline testing and can be carried out in real time. This overcomes the drawback of offline testing.

In the industry, online PD testing is carried out using two devices; a handheld device (called surveyor by Emerson) and a portable PD test unit. The primary use of the handheld unit is mainly to identify critical system components for PD testing. Usually, significant PD activity is prevalent in medium and high voltage system components. Effective prescreening ensures testing of critical components and also aides the process of formulating a test plan which will focus on testing of only necessary or critical system components.

Once prescreening is done, periodic PD measurements are taken using non-invasive sensors like high frequency current transformer (HFCT) sensors, transient earth voltage sensors, or airborne acoustic sensors. For critical areas along the cable that cannot be accessed with ease, certain sensors are permanently mounted for online monitoring. Periodic PD monitoring will help predict the trend of partial discharge occurrences over a period of time.

However, online PD testing has its drawbacks. It cannot detect occurrences of PD at voltages above the normal operating range. Certain approaches can only identify discharges as an occurrence between two sensors. Also, sensitivity assessment is usually not possible in online testing.

2.2 Cable Fault Location Detection Techniques

Now that the methods to diagnose cable insulation defects have been discussed, one common drawback of the methods discussed earlier is their inability to determine the location of the fault/defect. With the growing importance for underground power systems over the years, locating a cable fault has become an important issue that needs to be addressed to ensure the reliability of power supply to consumers.

Cable fault detection can be carried out online or offline. Online methods are based on the analysis of recorded fault signals while the cable is connected to the power system. In contrast, offline methods require the cable to be disconnected from the power system. They deal with injecting external test signals into the cable to detect the cable fault location. However, since their application requires disconnection from the grid, they are often referred to as post fault analysis.

2.2.1 Offline Testing Methods

Offline methods are found to be highly accurate and are chosen appropriately on the basis of cable installation requirements, length and size of the cable. Some of the existing offline techniques that will be discussed are time domain reflectometry (TDR), frequency domain reflectometry (FDR), time and frequency domain reflectometry (TFDR) and partial discharge (PD). Some methods demand skilled technicians while other methods, like the thumpers method can damage the cable during testing. Often, combinations of these methods are used for higher accuracy.

(i) Pulse Reflection Test using TDR method

The TDR method is a well-established and extensively used testing method to establish the total length of a cable and distance of cable faults [15]. This method is

primarily based on reflections of energy pulses that propagate through the cable. These pulses are transmitted to the cable by a time domain reflectometer. Owing to recent developments in this technique, it is possible to connect to one end of the cable, visualize its interior and measure distance to changes in the cable [16]. This technique provides a good insight on the characteristic impedance of the line and also shows both the position and nature (resistive, inductive, or capacitive) of any discontinuity along the cable [17].

The cable model is assumed to be based on the equivalent pi transmission line model and consists of resistance, inductance and capacitance. A voltage generated at the source will travel along the cable with the phase angle lagging the voltage by an amount β per unit length. Additionally, the voltage will decrease by an amount α per unit length due to the series resistance and shunt conductance of the cable. The propagation constant (γ) can be expressed as

$$\gamma = \alpha + j\beta = \sqrt{(R + j\omega L)(G + j\omega C)} \tag{2.2}$$

Where,

α = attenuation in nepers per unit length, and

β = phase shift in radians per unit length.

The velocity at which the voltage travels along the cable is given by

$$v_\rho = \frac{\omega}{\beta}$$

The voltage and current at any distance 'x' along an infinitely long cable can be expressed in terms of the propagation constant as follows

$$V_x = V_{in}e^{-\gamma x} \; and \; I_x = I_{in}e^{-\gamma x} \tag{2.3}$$

The condition of the transmission system is indicated by the ratio of this reflected wave to the incident wave. This ratio is called the voltage reflection coefficient (ρ) and is related to the transmission line impedance

$$\rho = \frac{V_r}{V_i} = \frac{Z_L - Z_O}{Z_L + Z_O} \tag{2.4}$$

Where,

Z_L = Impedance of the cable,

Z_O = Characteristic impedance,

V_i = Incident voltage, and

V_r = Reflected voltage.

A setup of the time domain reflectometer is shown in Fig. 2.3. A positive-going incident wave, applied to the transmission system under test, is generated using the step generator. The wave travels down the cable at the propagation velocity of the cable. If the load impedance is equal to the characteristic impedance of the cable ($V_r = 0$), no wave is reflected. Only the incident wave is recorded by the oscilloscope. However, if a mismatch exists at the load ($V_r \neq 0$), a part of the incident wave that is reflected will appear on the oscilloscope, algebraically added to the incident wave. Both these cases are depicted in Fig. 2.4 (a) and (b) respectively.

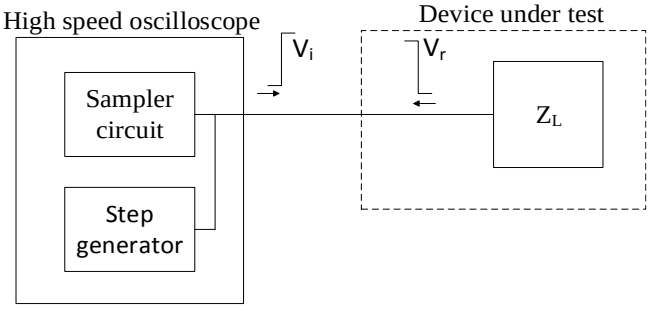

Fig. 2.3 Functional Block Diagram for a Time Domain Reflectometer [17].

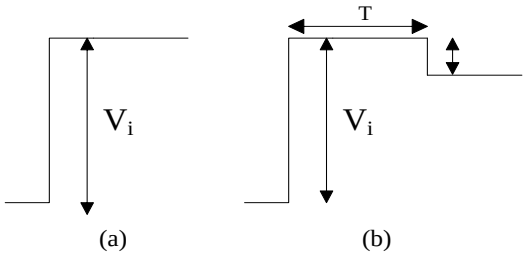

Fig. 2.4(a) Oscilloscope Display when $V_r = 0$, (b) Oscilloscope Display when $V_r \neq 0$ [17].

An important application of TDR deals with identifying discontinuities along the cable. Consider the system shown in Fig. 2.5. Let us examine the case when two cables of characteristic impedance Z_o are joined by a connector. Assuming the connector adds a small inductance in series with the cable, the system is analyzed based on the method mentioned above.

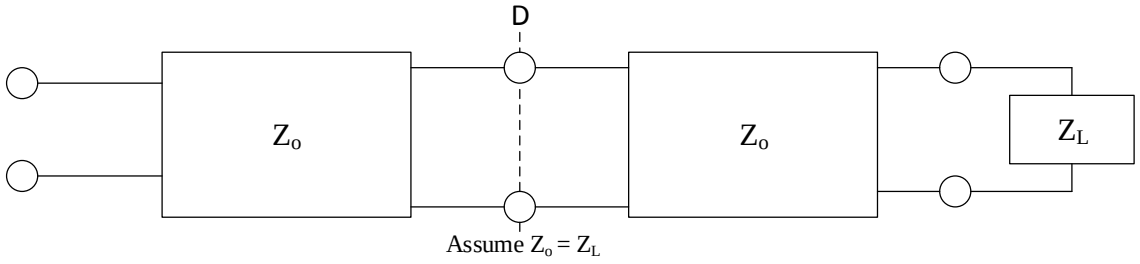

Fig. 2.5 Discontinuity along a Transmission Line [17].

Everything right of 'D' is treated as an equivalent impedance in series with an inductance, called the effective load impedance of the system at 'D' shown in Fig 2.6 (a).

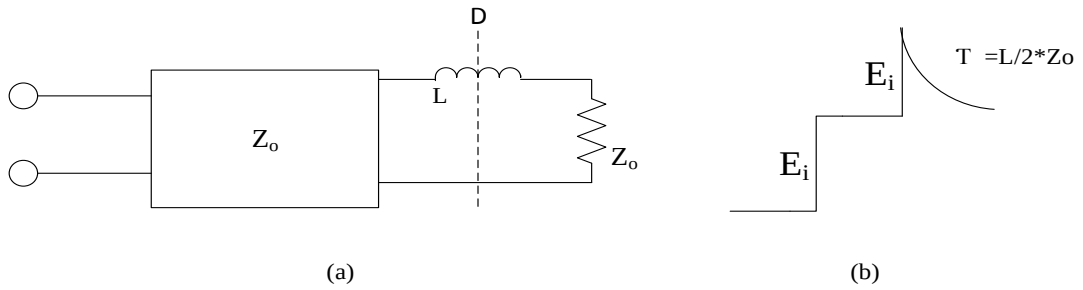

Fig. 2.6(a) Equivalent Circuit Representation, (b) Special Case of Series R-L Circuit [17].

The pattern on the oscilloscope is shown in Fig. 2.6 (b), which is a special case of a series RL circuit. One advantage of the TDR method is its ability to handle a situation involving multiple discontinuities.

Time domain reflectometry can also be applied to cases relating to losses in a transmission line. Cases when the series loss dominates will reflect a voltage wave with an exponentially rising characteristic, while those with shunt losses will reflect an exponentially decaying characteristic. For the case of series losses, the line looks more like an open circuit as time goes on since the voltage wave traveling down the line accumulates more series resistance to force current through. In the case of shunt losses, the input eventually looks like a short circuit because the current traveling down the line sees more accumulated shunt conductance to develop a voltage across [17].

(ii) Frequency Domain Reflectometry (FDR) method

The frequency domain reflectometer (FDR) technique can be used to determine cable length and location of faults based on the phase shift between the incident and reflected signal [18]. The reflected signal is digitized and the Discrete Fourier Transform (DFT) is used to estimate the location of discontinuities along the cable. The use of digital signal processing (DSP) techniques in this method improves the resolution and accuracy of measurements compared to the TDR method.

First, a case is considered where the cable under test has only one fault. The incident signal travels along the cable till it reaches the end or a fault point where the impedance changes. The signal, reflected with all or a part of the total energy of the incident signal, is received at the transmitter. The reflected signal has a phase difference with respect to the transmitted signal. The maximum cable length that can be measured is limited by the frequency step size and Nyquist criterion,

$$L_{max} = \frac{v_p}{4\,\Delta f} \tag{2.5}$$

For a frequency step of 20 kHz and cable propagation velocity of approximately two-thirds the speed of light, cable lengths upto 2.5 km can be tested. The accuracy of the cable length (L_{cable}) measurement is governed by the resolution of the DFT with the number of points in the DFT expressed as 'npts' [18],

$$L_{cable} = \frac{v_p}{2\,(npts)\,\Delta f} \tag{2.6}$$

When compared to the TDR method, the FDR method provides greater sensitivity and accuracy. The location of faults can be accurately detected. However, the FDR method cannot distinguish between different types of faults which is a shortcoming of this technique.

(iii) Time and Frequency Domain Reflectometry (TFDR) method

The TFDR method works on a similar principle as that of the TDR method except the fact that it uses a linear chirp incident signal with a Gaussian envelope for the cable under the test. An arbitrary waveform generator (AWG) produces the incident signal which travels along the cable. The incident signal is reflected back at the end of the

cable or point of a fault with all or a part of its energy. A coupler is used to separate the reflected signal from the incident signal.

The cross-correlation between the incident and reflected signal, expressed in Eq. (2.7), can be used to estimate the location of faults along the cable length [18].

$$r_{xy}(n) = r_{xx}(n) \otimes h(n) + r_{xn}(n) = r_{xx}(n) \otimes h(n) \quad (2.7)$$

Where, r_{xy} is the cross correlation between the incident and reflected signal, $\otimes$ denotes convolution; n is the shift parameter number; r_{xx} is the autocorrelation of incident signal; $h(n)$ is the transfer function of the cable system; r_{xn} is the cross-correlation between incident signal and noise, its value is zero in this case.

Although the use of a time-frequency cross-correlation functions has its advantages of improving sensitivity and accuracy of measurements, it suffers from several drawbacks. First, the use of the AWG with high frequency bandwidth makes it more expensive compared to the TDR method. Secondly, TFDR cannot distinguish between different fault types. Third, cables tend to have higher attenuation at higher frequencies which limits the measurement range. Hence, TFDR can be applied for detection and localization of faults only on short cables.

2.2.2 Online Testing Methods

The offline methods discussed earlier dealt with fault location detection by disconnecting the system from the grid. Hence, they are incapable of detecting faults occurring in real time. Many of the fault detection techniques are based on time and frequency domain analysis of conventional power system signals like voltage and current. In order to improve the reliability of these techniques, a sufficiently high sampling rate is chosen for analysis.

Online cable fault location detection can be classified under two main categories; impedance based and travelling wave based methods [19].

(i) Impedance based methods

Impedance based fault methods are particularly characterized by fast response, ease of application, stability and cost effectiveness. Estimation of fault location using this method is carried out by comparing the change in impedance during a fault to pre-established line parameters under normal operating conditions. Impedance based methods can either be single ended or two ended.

Single or one ended methods estimate the fault location by calculating the impedance by looking into one end of the line. In order to ensure accurate estimation, all the phase to ground voltage and current values must be measured. Line to line voltage measurements will help in locating phase to phase faults [20]. Two ended methods are based on analysis carried out by looking from both ends of the cable.

The most popular impedance based fault location methods are simple reactance method (one ended), Takagi method (one ended), modified Takagi method (one ended) and negative sequence method (two ended).

- Simple Reactance Method

The simple reactance method is a one ended method based on the measurement of a short circuit loop at the power frequency, in a solidly grounded network [4]. The ratio of the measured reactance to the total reactance of the transmission system is proportional to the fault distance. The load is assumed to be zero prior to the fault. With reference to Fig. 2.7, which represents the circuit for a faulted power system, it can be said that

$$V_A = l\, Z_m I_A + R_F I_F \qquad (2.8)$$

For a particular phase to ground fault, V_s will represent the phase to ground voltage (say V_{ns}). As the name suggests, this method focuses only on the imaginary part and minimizes the effect of the resistance term. Eq. (2.8) is divided throughout by I_A and the $R_F I_F / I_A$ term is neglected. The imaginary part is now solved to determine the value of l.

$$\mathrm{Im}(V_A/I_A) = \mathrm{Im}(l\, Z_m) = l\, X_m$$

$$l = \frac{\mathrm{Im}(V_A/I_A)}{X_m} \tag{2.9}$$

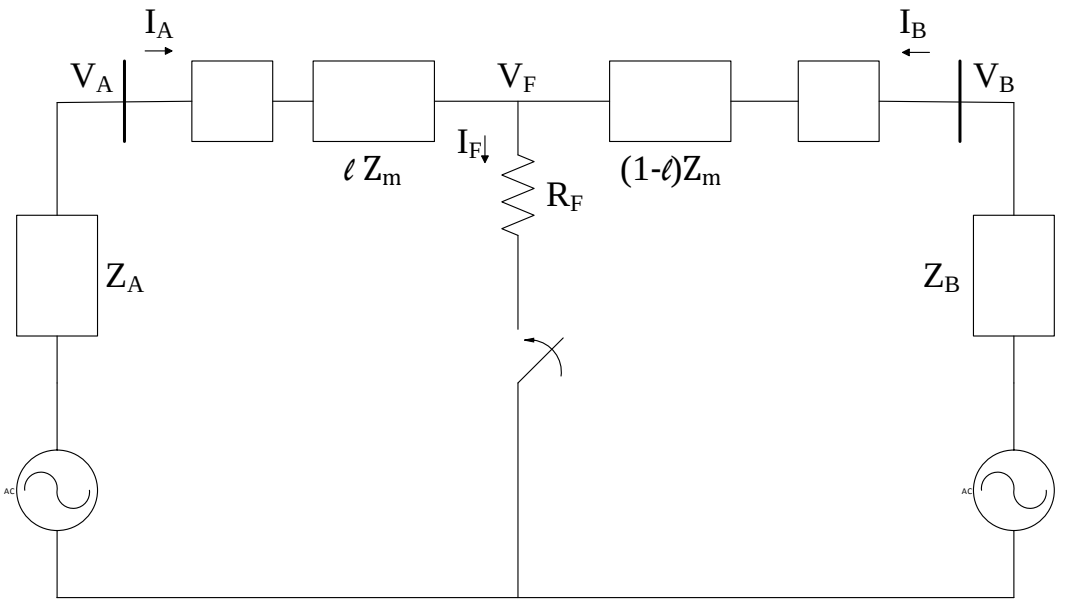

Fig. 2.7 Circuit Diagram for a Line Fault [20].

The accuracy of estimating the fault location depends on how accurately the impedance of the system is calculated. A number of reasons like zero sequence mutual coupling, system homogeneities and inaccurate relay measurements can affect impedance measurement and thus introduces some error in the fault location estimate [21].

- Takagi Method

The Takagi method is an improvement from the simple reactance method. It reduces the effect of load flow and also minimizes the effect of the fault resistance. This method is based on pre-fault and fault data.

$$V_A = l\, Z_m I_A + R_F I_F \tag{2.10}$$

The superposition current I_{sup} is used to find a term in phase with the fault current, I_A. I_{pre} is the pre-fault current.

$$I_{sup} = I_A - I_{pre}$$

Both sides of Eq. (2.10) are pre-multiplied by I_{sup}^* and solved for l by considering only the imaginary part of the expression.

$$\mathrm{Im}\left(V_A I_{sup}^*\right) = \mathrm{Im}\left(l\, Z_m I_A I_{sup}^*\right) + \mathrm{Im}\left(R_F I_F I_{sup}^*\right) \tag{2.11}$$

Now, when I_A is in phase with I_F, the term with I_F can be neglected and thus the fault location can be estimated as

$$p = \frac{\mathrm{Im}\left(V_A I_{sup}^*\right)}{\mathrm{Im}\left(Z_m I_A I_{sup}^*\right)} \tag{2.12}$$

The success of the Takagi method is based on the above described assumption which holds true for an ideal homogeneous system [20].

- Modified Takagi Method

The modified Takagi method is an improvement over the Takagi method. It is also called the zero sequence angle method with angle correction. The difference being that this method makes use of the zero sequence current ($3\, I_0$) instead of the

superposition current for ground faults. Unlike the Takagi method, this method does not require the pre-fault data.

Another important aspect of this method is that it allows for angle correction, i.e., if the impedance of the system is known, the zero sequence current angle is adjusted by Θ to improve the estimate of the fault location. The expression to estimate the fault location is given in Eq. (2.14).

$$\frac{I_F}{3I_0} = \frac{Z_{0A} + Z_m + Z_{0B}}{(1-l)Z_m + Z_{0B}} = A\angle\Theta \tag{2.13}$$

where Θ is the angle between zero-sequence current I_0 and fault current I_F. The distance to the fault can be calculated based on the expression given by

$$l = \frac{\mathrm{Im}\left(3V_A I_0^* e^{-j\Theta}\right)}{\mathrm{Im}(3Z_m I_A I_0^* e^{-j\Theta})} \tag{2.14}$$

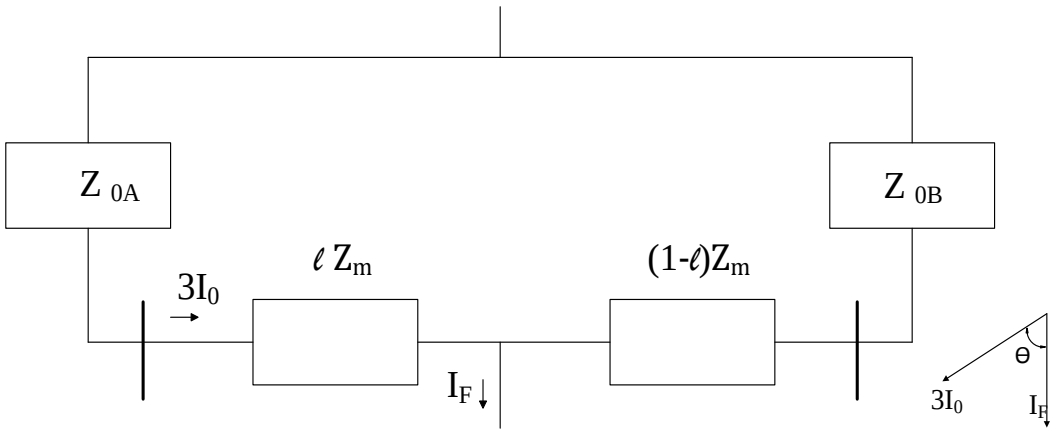

Fig. 2.8 Zero-Sequence Current Angle Correction for a Known Source Impedance [20].

- Two ended negative sequence method

The negative sequence method, classified as a two ended method, is a relatively new method introduced in 1999 [20]. It makes use of negative sequence

quantities from all line terminals to estimate fault location in the case of unbalanced faults. Using negative-sequence quantities negates the effect of pre-fault load, fault resistance, zero-sequence mutual impedance and zero-sequence infeed from transmission line taps [20]. Unlike single ended methods, the negative-sequence method requires the source impedance.

Data alignment is not a requirement since the algorithm employed at each line end uses the following from the remote terminal (which do not require phase alignment) [20]

- Magnitude of negative-sequence current I_2, and

- Calculated negative-sequence source impedance $Z_2\angle\theta_2$.

The negative sequence circuit is shown in Fig. 2.9. It can be observed from Fig 2.9 that the negative-sequence fault voltage (V_{2F}) is the same when viewed from all ends of the protected line.

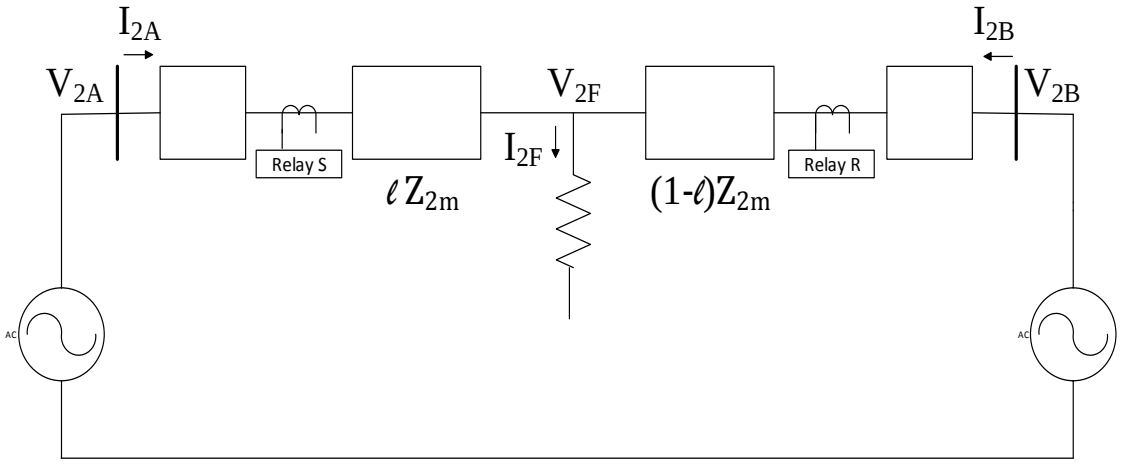

Fig. 2.9 Negative-Sequence Network for a Single Line to Ground Fault [20].

At relay S, $$V_{2F} = -I_{2A}(Z_{2A} + pZ_{2m}) \quad (2.15)$$

At relay R, $$V_{2F} = -I_{2B}(Z_{2B} + (1-p)Z_{2m}) \quad (2.16)$$

Eliminating V_{2F} from Eq. (2.15) and Eq. (2.16),

$$I_{2B} = I_{2A}\frac{Z_{2A} + pZ_{2m}}{Z_{2B} + (1-p)Z_{2m}} \quad (2.17)$$

The magnitude of Eq. (2.17) is taken in order to prevent alignment of data sets of relays R and S. A number of fault location examples in transmission systems is discussed in [20].

(ii) Travelling Wave Based Methods

In the past, underground cable fault location identification based on travelling wave methods was primarily adopted for de-energized cable testing. The need for specific instrumentation was required to detect the reflected voltage from the fault. However, subsequent developments in this field make use of the travelling wave transients that develop during a fault due to high voltage which causes an arc at the fault point [22].

The drawbacks of the impedance or reactance based methods have led to the search for an alternative travelling wave based method to locate cable faults. However, in the recent past, though many methods have been proposed and developed in literature, very few have reached the stage of real time implementation with only one of the methods, type C, which is currently available commercially. The classification of cable fault locators into type A, B, C and D is primarily based on their mode of operation.

Types A and D depend on the travelling wave transients produced during a fault and hence do not require an external pulse. Type A is a single ended method and

requires a sufficiently large discontinuity to reflect the incident signal back from the fault. On the other hand, type D is a double ended method which detects the reflected signal from the fault point at both ends of the cable using synchronized timing circuits.

Types B and C are pulse driven and hence need appropriate pulse generating circuitry. Type B is a double ended method and is further classified into types B1, B2 and B3. Types B1 and B2 inject a pulse to the opposite end of the cable as soon as the arrival of a fault generated transient is detected, whereas type B3 injects a pulse into the circuit after a specific time interval from the time of initiation of the fault. Type C is a single ended method where the reflection of the pulse injected by the unit itself is used to locate a fault.

- Travelling Wave Based Fault Location Algorithms

The travelling wave-based fault location methods are primarily useful in case of crossbonded cables. Their implementation involves higher costs when compared to conventional power frequency methods. This is due to the requirement of high frequency data acquisition systems and highly accurate common time reference at both line ends. In spite of the high cost involved, this method is still a feasible option since it is fairly straightforward and is independent of any system parameters which affect other fault location algorithms adversely. The detection of fault location based on travelling wave methods for crossbonded cables, though not well established, is considered more complex than fault detection in overhead lines or non-crossbonded cables. This is because of the additional reflections created due to the process of crossbonding [23].

(iii) Application of artificial intelligence techniques for fault location

Artificial Neural Networks (ANN), used for pattern recognition, are trained using a specific system models in order to identify certain behavior. Nonlinear mapping and parallel processing are some capabilities of neural networks that can be particularly useful for fault location if trained in the right manner. The use of ANN algorithms can be of good use in case of multi ended transmission and distribution system with laterals. Fuzzy logic, which is useful for treating ambiguous, imprecise, noisy, or missing data, is often used in conjunction with ANN for fault location techniques [23]. There are several literatures that have proposed the application of ANN, fuzzy logic or a combination of both for power system protection schemes. For example, [24] proposes a single ended algorithm for determining fault location in a 400 kV overhead transmission line using the concept of ANN. The inputs to the ANN are pre fault and post fault voltage and current values. The output of the algorithm gives the fault resistance and distance to the fault. Results are compared to traditional fault location algorithms and it is seen that proper training of the ANN will ensure its adaptation to variations in fault resistance and source impedances.

The application of ANN for overhead line fault location detection has been addressed in many literatures. However, not much extensive work has been done with respect to fault location problems in cross bonded cables. As mentioned earlier, the ANN algorithm learns through previous experience (supervised learning). Therefore, development of fault location methods for underground cables should be possible using those already proposed. The important aspect of training the ANN is the reliability and credibility of the data from proposed methods. None of the proposed models have reached the real time testing and deployment phase and the use of oversimplified models,

though useful to attain good results, cannot be extended to real world situations. The precision with which fault behavior can be predicted in crossbonded cables will determine any final recommendations made with respect to ANN applications [24].

This chapter presented a brief overview of methods currently in practice for online and offline monitoring of power cables. Although some of the methods discussed are widely used in the industry, there is still a need for an effective cable monitoring and fault location method. Chapter 3 will propose an online monitoring and fault location methodology for underground power cables. A theoretical base for this method will be presented followed by a series of computer simulations in Chapter 4 to validate the theory.

CHAPTER 3

PROPOSED METHODOLOGY

This chapter introduces the proposed cable monitoring methodology with theoretical studies. The studies are based on the frequency dependent behavior of cable voltage and current signals. First, theoretical studies are reviewed on the frequency dependence of the transmission system model under consideration. Frequency dependence refers to the resonant frequency characteristic of the given system. Conventional power signals are utilized to study the behavior of resonant frequencies under various conditions.

The behavior of resonant frequencies is explained for different system conditions with the help of analytical derivations obtained in [4]. One such anomalous condition considered is a single line to ground fault. Initially, a simplistic system is considered in order to establish the proposed methodology. Once this is evaluated, a realistic model, closely representing actual system conditions is considered for analysis. A detailed description of the two different cases evaluated will be discussed in subsequent sections. This is followed by the theoretical analysis of resonant frequency behavior under normal conditions and in the case of a single line to ground fault condition.

3.1 Introduction

Every transmission system such as overhead lines or underground cables have electrical parameters (i.e., resistance, inductance and capacitance) which vary depending on certain factors. One such factor is the length of the line or cable. Resonant frequencies for a system can be obtained by computing the power spectral density (PSD) of voltage and current signals measured from the system. These resonant frequencies are unique for every system and depend on these electrical parameters. Any change in these parameters

due to faults in the system, load changes or any anomalous conditions leads to changes in the behavior of the resonant frequencies.

The main idea of the proposed methodology is based on observing the resonant frequencies under various system conditions. The resonant frequencies measured under normal operating conditions are taken as the reference. Any deviation from the reference is an indication of an abnormal system condition. This is particularly helpful for the prediction of fault location in underground cables which will be discussed later in detail. Thus, online resonant frequency analysis is an effective way of monitoring and understanding system behavior.

3.2 Electrical Parameters

3.2.1 Overhead Lines

Before evaluating the underground cable system, electrical parameters of the overhead transmission system are first reviewed. The electrical parameters of a three phase, transposed overhead transmission line can be expressed as [25]

$$\text{Resistance,} \quad R_x = \mathrm{R}_{75}\ [\Omega/\mathrm{km}] \tag{3.1}$$

$$\text{Inductance,} \quad L_x = \frac{\mu_0}{2\pi} \ln\left(\frac{\mathrm{GMD}}{\mathrm{GMR}}\right)\ [\mathrm{H/km}] \tag{3.2}$$

$$\text{Capacitance,} \quad C_x = \frac{2\pi\varepsilon_0}{\ln\left(\frac{\mathrm{GMD}}{\mathrm{r_{bund}}}\right)}\ [\mathrm{F/km}] \tag{3.3}$$

Where,

GMD - conductor geometrical mean distance = $\sqrt[3]{D_{ab} \cdot D_{bc} \cdot D_{ca}}$

GMR - conductor geometric mean radius = $\sqrt{d_c \cdot GMR_c}$ for a 2 conductor bundle

r_{bund} - equivalent radius of the conductor = $\sqrt{d_{bund} \cdot r_0}$

D_{ab}, D_{bc}, D_{ca} represent the distance between the phases; d_c is the distance between the conductors; GMR_c is the GMR of the conductor; d_{bund} is the distance between the bundles; r_0 is the conductor radius and R_{75} is the resistance of the conductor at 75°C.

3.2.2 Underground Cable

In comparison to overhead lines, underground cables have higher capacitance. The high capacitance in underground systems is a source of complex electromagnetic phenomena that results in energizing or de-energizing over-voltages in underground transmission systems.

The resistance of underground cables is expressed as [26]

$$R_x = R_{AC} = R_{DC}\left[1 + y\left(k_s + k_p\right)\right] \ [\Omega/\text{km}\ ] \tag{3.4}$$

where R_{AC} and R_{DC} are the equivalent AC and DC circuit resistances, respectively. k_s is the skin effect factor; k_p is the proximity effect factor; and y is a constant ($y = 1$ for 1, 2 and 3 core cables, $y = 1.5$ for pipe-type cables) [27].

The inductance of underground cables is calculated as [28]

$$L_x = \frac{\mu_0}{2\pi} ln\left(\frac{r_o}{r_i}\right) \tag{3.5}$$

where r_o is the outer radius of the phase screen insulator, and r_i is the outer radius of the phase conductor including the conductor shield or outer radius of the phase insulator.

The capacitance is calculated as [29]

$$C_x = 0.024 \frac{\varepsilon_r}{log\left(\frac{D}{d}\right)} \quad [\mu F/km] \tag{3.6}$$

where ε_r is the relative permittivity of the insulation between the sheath and earth, D is the outer diameter of the phase screen insulator and d is the inner diameter of the phase screen insulator.

3.3 Theoretical Analysis

This section establishes the theoretical base for the proposed methodology. Analytical expressions for the frequency dependence of the transmission system models are analyzed. The frequency dependence of transmission models is studied based on frequency domain analysis of conventional power signals. Two cases are evaluated. 'Case a' considers a simplistic system which consists of a source delivering power to a load through a cable as shown in Fig. 3.1. 'Case b' deals with a more realistic scenario by considering the presence of a transformer in the system.

3.3.1 Case a : Transmission Line Only

First, a simplistic system is considered. The system consists of a source (V_S) that delivers power to a load (Z_L) through an underground cable as shown in Fig. 3.1. This case is evaluated in order to verify the theory on resonant frequencies and provide a base for the proposed methodology.

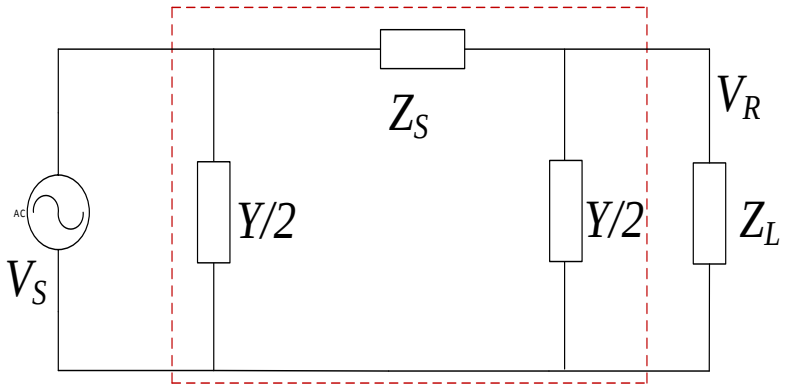

Fig. 3.1 Distributed Parameter Model for a Transmission System.

The literature on transient analysis verifies that the equivalent pi model shown in Fig. 3.1 is the best representation of the frequency dependent behavior of a transmission system [30]. The equivalent pi model distributes the electrical parameters along the length of the line.

The system impedance and shunt admittance are given by

$$z = R_x + j\omega L_x, \qquad y = j\omega C_x \tag{3.7}$$

where R_x, L_x and C_x represent the resistance, inductance and capacitance per unit length, respectively.

For a cable of length l, the series and parallel impedances are given by [31]

$$Z_S = Z_c \sinh(\gamma l) \tag{3.8}$$

$$Z_P = \frac{tanh(\gamma l/2)}{Z_c} \tag{3.9}$$

where $\gamma = \sqrt{(R_x + j\omega L_x) j\omega C_x}$ is the propagation constant and the characteristic impedance is $Z_c = \sqrt{(R_x + j\omega L_x)/j\omega C_x}$.

The transfer function for the cable transmission system without the load is given by

$$H_C = \frac{V_R}{V_S} = \frac{Z_P}{Z_S + Z_P} = \frac{1}{\cosh(\gamma l)} \tag{3.10}$$

In the s-domain,

$$H_C(s) = \frac{V_R(s)}{V_S(s)} = \frac{1}{\cosh\left(\sqrt{(R + sL)sC}\right)} \tag{3.11}$$

The resonant frequencies are obtained by solving for the roots of the denominator in Eq. (3.11). The roots obtained are [4]

$$s_{nC} = -\frac{R}{2L} \pm j\sqrt{\frac{\left((2n-1)\pi\right)^2}{4LC} - \frac{R^2}{4L^2}}, \qquad n = 1, 2, 3, \ldots \tag{3.12}$$

Typically, $1/(LC) \gg (R/L)^2$, therefore, approximate values of the roots are

$$s_{nC} \cong -\frac{R}{2L} \pm j\frac{(2n-1)\pi}{2\sqrt{LC}}, \qquad n = 1, 2, 3, \ldots \tag{3.13}$$

The resonant peak appears when the frequency is equal to the imaginary part of Eq. (3.13). Therefore, the approximate resonant frequencies are [32]

$$\omega_{rn_C} \cong \frac{(2n-1)\pi}{2\sqrt{LC}}, \qquad fr_{nC} \cong \frac{(2n-1)}{4\sqrt{LC}}, \qquad n = 1, 2, 3, \ldots \tag{3.14}$$

The resonant frequencies obtained follow odd multiples, i.e., the second peak is three times the first peak and the third peak is 5 times the first peak and so on. An extensive step by step procedure for deriving the expression for the resonant frequencies is presented in [4].

3.3.2 Case b : Transmission Line and Transformer

This case evaluates a more realistic scenario approximately representing actual system conditions. It is known that every power system consists of a transformer to provide different voltage levels in the system. In this case, a step up transformer is connected to the source as shown in Fig. 3.2.

This section studies the behavior of resonant frequencies for a transformer connected power system and the differences observed in the resonant frequencies when compared to ‘Case a’, i.e., the no transformer case.

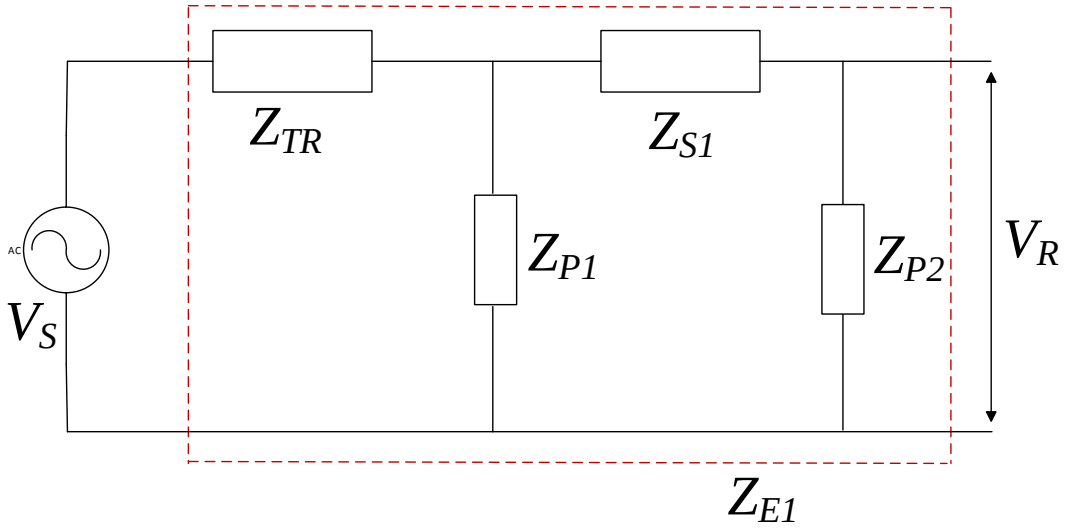

Fig. 3.2 Equivalent Pi Model for the Transformer Connected Transmission System.

The system model for 'Case b' is shown in Fig. 3.2. The transformer impedance is given as $Z_{TR} = R_{TR} + j\omega L_{TR}$. The equivalent impedance Z_{E1} can be expressed in the transfer function form as

$$Z_{E1} = \frac{1}{\frac{1}{Z_{S1}+Z_{P2}} + \frac{1}{Z_{P1}}} = \frac{Z_{P2}}{\frac{Z_{P2}}{Z_{S1}+Z_{P2}} + \frac{Z_{P2}}{Z_{P1}}}$$

$$= \frac{Z_{P2}}{H_{S1} + \frac{Z_{P2}}{Z_{P1}}} = \frac{Z_{P2}}{Z_{P1}H_{S1} + Z_{P2}} \tag{3.15}$$

The transfer function for the transformer connected system can be obtained as follows

$$H_T = \frac{V_R}{V_S} = \frac{Z_{E1}}{Z_{TR}+Z_{E1}} H_{S1} \quad \text{where, } H_{S1} = \frac{Z_{P2}}{Z_{S1}+Z_{P2}}$$

The transfer function can be represented in terms of hyperbolic trigonometric functions obtained using the ABCD parameters of the equivalent pi model. The expression is derived in detail in [4] and is expressed as

$$H_T = \frac{V_R}{V_S} = \frac{1}{Z_{TR}\frac{1}{Z_c}sinh(\gamma l) + cosh(\gamma l)} \tag{3.16}$$

A detailed step by step procedure for obtaining the expression for the transfer function and resonant frequencies is presented in Appendix D of [4]. From [4], it is seen that for higher frequencies, the effect of the $\cosh(\gamma l)$ is very small and hence for frequencies above 500 Hz, it can be assumed that $Z_{TR}\frac{1}{Z_c}\sinh(\gamma l) \gg \cosh(\gamma l)$. The simplified transfer function based on the above assumption is

$$H_T = \frac{V_R}{V_S} = \frac{1}{Z_{TR}\frac{1}{Z_c}sinh(\gamma l)} \tag{3.17}$$

Similar to Eq. 3.14, the resonant frequencies for the transmission system including the transformer are found to be

$$\omega_{rn_T} \cong \frac{n\pi}{\sqrt{LC}}, \qquad fr_{nT} \cong \frac{n}{2\sqrt{LC}}, \qquad n = 1, 2, 3, \ldots \tag{3.18}$$

In the previous section, Eq. (3.14) showed the resonant frequencies for the system without the transformer. Comparing Equations (3.14) and (3.18), it can be seen that for the case of the transformer connected system, the fundamental frequency is twice that of the system without the transformer. Subsequent peaks are shifted by a specific factor based on Eq. (3.18). Another observation is that the difference of the resonant frequencies for systems with and without the transformer is the same as the resonant frequency for 'Case a' as expressed in Eq. (3.19).

$$frn_T - frn_C \cong \frac{n}{2\sqrt{LC}} - \frac{(2n-1)}{4\sqrt{LC}} = \frac{1}{4\sqrt{LC}}, \qquad n = 1, 2, 3, \ldots \tag{3.19}$$

3.4 Behavior of Resonant Frequencies

The resonant frequencies are unique to every system and can be used as a means to monitor the condition of a cable power system. Condition monitoring can involve observing cable parameters under varying load conditions or in the presence of cable faults. However, in order to understand the behavior of resonant frequencies under anomalous conditions, it is necessary to observe their behavior under normal operating conditions. The resonant frequencies are obtained by computing the power spectral density (PSD) of voltage and current signals from the system. They are evaluated for two conditions. This section deals with studying the behavior of resonant frequencies under normal operating conditions and an anomalous condition (single line to ground fault in this case).

3.4.1 Normal Operating Conditions

The expression for the resonant frequencies for this case is given in Eq. (3.18). Inherent noise refers to the fluctuations present in a power system which distort the signals. Some examples of noise sources include electromagnetic interference, power electronic circuitry or large motors. This section will focus on observing the power spectral density of the voltage signal with and without the presence of noise in the system. The importance of noise in the system can be observed in terms of extraction of distinct resonant frequencies. It is to be noted that this case evaluates the transformer connected power system described in Section 3.3.2.

The resonant frequencies of the system may be identified using frequency domain analysis of the transfer function in Eq. (3.17). Practical conditions require the need for input frequency signals to determine the cable frequency response. This could be made

possible by the injection of artificial frequency signals into the system. However, injection of these artificial signals leads to additional cost and unexpected distortions in the power system.

Therefore, for the purpose of simulation, our focus is on incorporating the inherent fluctuations (i.e., signal noise) present in the system by injecting normally distributed random noise at the input. In other words, the inherent noise fluctuations serve as the driving input signal to determine the system transfer function. The frequency spectrums of the transfer function, input and output signals for the selected transformer connected underground power system are obtained for two different scenarios.

The system considered for analysis is based on the schematic shown in Fig. 3.2. The PSD plots are obtained by frequency domain analysis of the transfer function expressed in Eq. (3.17). First, the fast Fourier transform (FFT) of the voltage signal is computed and the magnitude square of the FFT gives the PSD of the voltage signal. The analysis is carried out in MATLAB. The use of a window function, which plays an important role in obtaining the PSD as will be discussed in Chapter 4, is not considered in this analysis.

In the first scenario, the ideal power source contains only the 60 Hz component and hence shows absence of resonant frequencies in the output signal spectrum shown in Fig. 3.3. The input spectrum is multiplied by a factor of 10^5 to avoid overlap with the output spectrum. Thus, the 60 Hz operational signal alone does not permit experimental determination of the system transfer function.

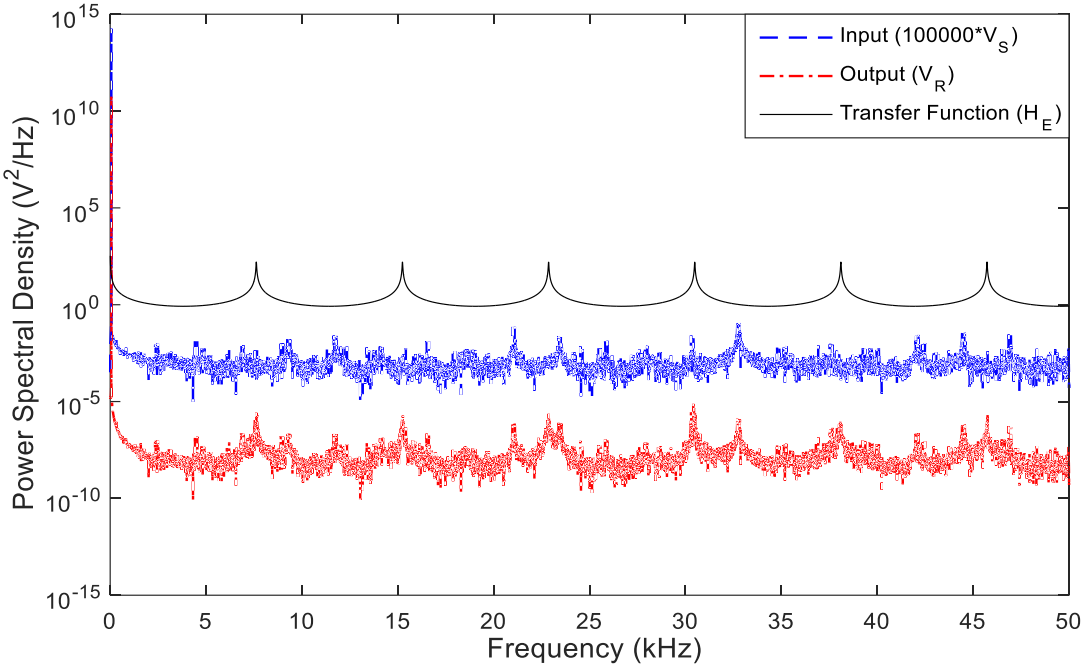

Fig. 3.3 Frequency Spectrums for No Noise Contained in the Input Voltage.

For the second case, 0.1% signal noise is injected into the system at the source to elicit the resonant frequencies. The percentage of noise injected is interpreted in terms of the peak source voltage, i.e., 0.1% noise indicates normally distributed noise with a magnitude of 0.1% of the peak source voltage. The term “injected noise” represents the existing inherent noise in the power system. It is observed from Fig. 3.4 that the output voltage signal clearly shows the presence of the resonant frequencies. The fundamental resonant frequency is found to be 7620 Hz. Therefore, depending on the presence or absence of noise in the system, it may be possible to extract the resonant frequencies through spectral analysis of voltage measurements. Thus, the presence of noise in the system is an important requirement for measuring distinct resonant frequencies. A similar analysis, carried out with the current signal, is presented in the next chapter.

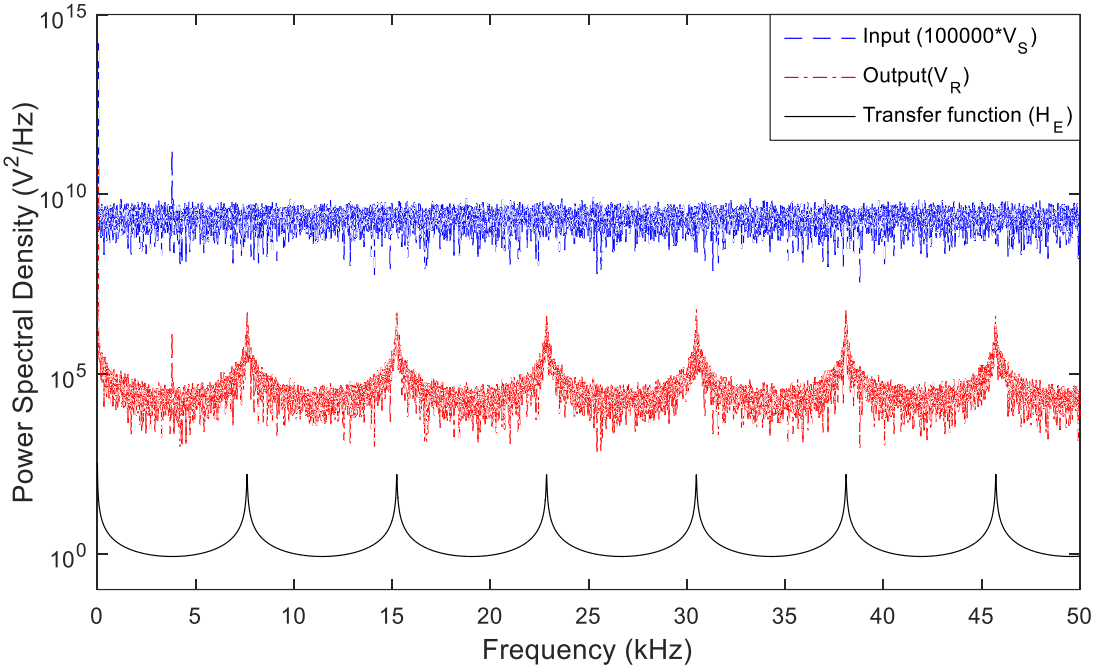

Fig. 3.4 Frequency Spectrums for 0.1% Noise Contained in the Input Voltage.

Figs. 3.3 and 3.4 are obtained for a data set length of 2^{12} points, i.e. 4096 data points. The data are sampled at 2 μs. Usually, any power of 2 can be chosen to define the number of data points. However, for the purpose of uniformity in analysis and simulations, the value in this thesis is fixed at 2^{12}. Another reason for choosing this particular value will be discussed during the analysis of actual power system signals in Chapter 5.

3.4.2 Single Line to Ground Fault

The presence of a fault in the system will affect the impedance of the network which in turn will cause changes to the resonant frequencies. This section studies the behavior of resonant frequencies in the presence of a single line to ground fault. Consider a case where a contingency in the form of a single line to ground fault is applied to the

system at a specific point along the length of the power cable. The equivalent circuit representation for the faulted power system is shown in Fig. 3.5.

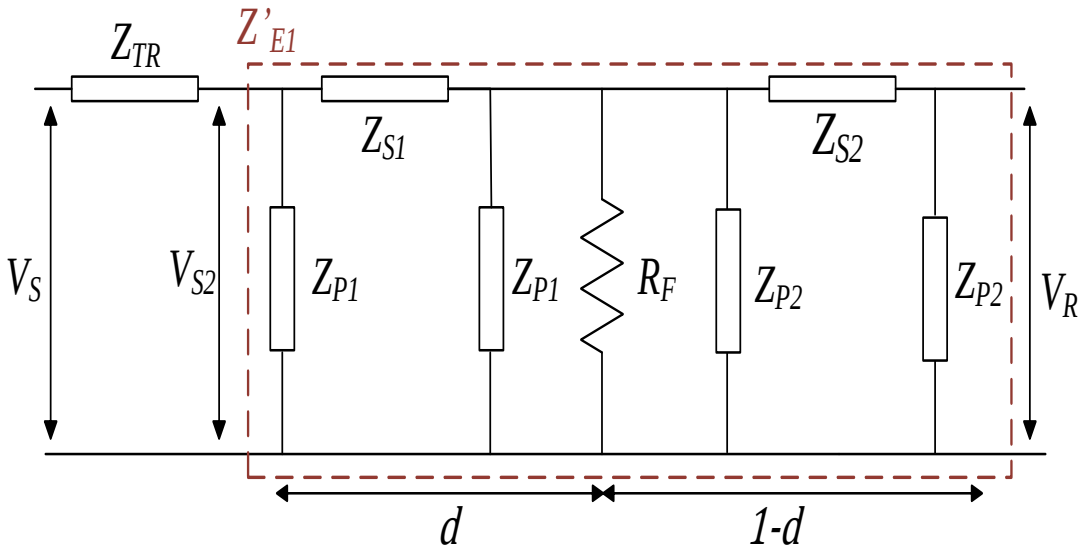

Fig. 3.5 Equivalent Circuit for the Faulted Power System.

The fault is applied by adding a fault resistance R_F at a fractional distance 'd' along the cable length. The expression for the transfer function of the system in Fig. 3.5 has been derived in detail in [4] and is expressed as

$$V_R = V_S H_{TF} = \frac{Z'_{E1}}{Z_{TR} + Z'_{E1}} V_S H_C \quad \ldots (3.20)$$

$$\frac{V_R}{V_S} = H_{TF} = \frac{Z'_{E1}}{Z_{TR} + Z'_{E1}} H_C \quad \ldots (3.21)$$

where H_{TF} is the transfer function for the faulted power system shown in Fig. 3.5, and H_C is the transfer function of the dashed region which represents the cable power system. A simplified expression for H_C in terms of hyperbolic trigonometric functions is [4]

$$H_C = \frac{1}{\cosh(\gamma l) + \frac{Z_c}{R_F}\sinh(d\gamma l)\cosh(\gamma(1-d)l)} \quad \ldots (3.22)$$

The resonant frequencies for the transformer connected system are obtained by solving for the roots of the characteristic equation and depend on the fault position as expressed in Eq. (3.22). The first term of Eq. (3.21), i.e., $\frac{Z'_{E1}}{Z_{TR}+Z'_{E1}}$, is a combination of the transformer impedance and the equivalent impedance of the dashed region in Fig. 3.5. The additional resonant frequencies resulting from this term lie beyond the frequency range of interest for this research and are hence not considered. Therefore, the roots of the denominator of Eq. (3.22) give the value of resonant frequencies for this case. The expression for the resonant frequencies is derived in detail in [4] and is given by

$$fr_{\mathrm{n}CF} \cong \frac{(2n-1)}{4\sqrt{LC}(1-d)} \quad \ldots (3\text{-}23)$$

A detailed study on the trend observed in the power spectrum for a faulted system for different fault positions is presented in the next chapter.

CHAPTER 4

ANALYSIS BASED ON COMPUTER SIMULATIONS

Now that the theory behind the resonant frequencies has been established, the system behavior is studied with the help of time domain simulations. This is primarily carried out to verify the theoretical results. The model utilized for the simulations is part of an actual power system. The analysis of actual power system data will be discussed in detail in Chapter 5. The model is built in Simulink and frequency domain analysis is carried out using code written in MATLAB.

Similar to the theoretical analysis, the behavior of the resonant frequencies is simulated for two cases. 'Case a' deals with frequency domain signal analysis for a simplistic system, i.e., considering only the cable section. This is done in order to verify the theory presented in Section 3.3.1. 'Case b' is a re-evaluation of 'Case a' with a transformer inserted in the circuit. This case assesses a more realistic scenario approximately representing actual system conditions. This case is implemented for two reasons. The first being to verify the effect of the transformer on the resonant frequencies as shown in theory. Secondly, the simulation data are compared with measured data obtained from the actual system. The system for both cases is modeled using the Sim power systems package in Simulink. The power spectral density (PSD) is computed in MATLAB using the periodogram function for the data exported from the workspace in Simulink. A RL series electrical load is connected at the end of the power cable.

Another important aspect discussed in this chapter is the effect of windowing on the PSD of system signals. The utilization of an appropriate window function has an advantageous effect on the PSD for both cases which will be discussed in detail.

4.1 Validation of Theoretical Analysis through Computer Simulations

The cable under consideration is a 154 kV, 1200 mm^2, 10.5 km long cross linked poly-ethylene (XLPE) underground power transmission cable located in South Korea. The cable parameters, for the 60 Hz system, calculated from the cable geometry are listed in Table 4-1. Detailed calculations for the cable parameters based on the formulae in Chapter 3 and cable geometry data are presented in Appendices A and B, respectively.

Table 4-1 Parameters of Underground Power Cable

Conductor diameter	39.08 mm
Inner / Outer radius of main insulator	21.54 mm / 38.54 mm
Spacing between conductors: (flat formation)	0.3 m
Resistance	0.019 Ω/km
Inductance	0.116 mH/km
Capacitance	335.6 nF/km
Propagation constant	$(5.1+ j25.2)\times10^{-3}$
Characteristic impedance	19.484 – j3.9347 Ω

4.1.1 Case a : Transmission Line Only

The system under consideration is represented schematically in Fig. 3.1. As mentioned earlier, a key requirement of this methodology is the presence of inherent noise in the power system. Since computer simulation programs do not account for noise in a system, the presence of noise in the system is simulated using a normally distributed random number (signal) generator and injected at the system source. The system is simulated under various noise levels ranging from 0.2% to 1% of the peak source voltage, i.e., 14.42 kV, in increments of 0.2%. This is carried out to determine the lowest noise level for discernible resonant frequencies. Also, simulating the system under different noise levels will give a reasonable idea of the noise level in the actual system when

comparing simulation and actual measurement data. Fig. 4.1 shows the system voltage signal for various noise levels.

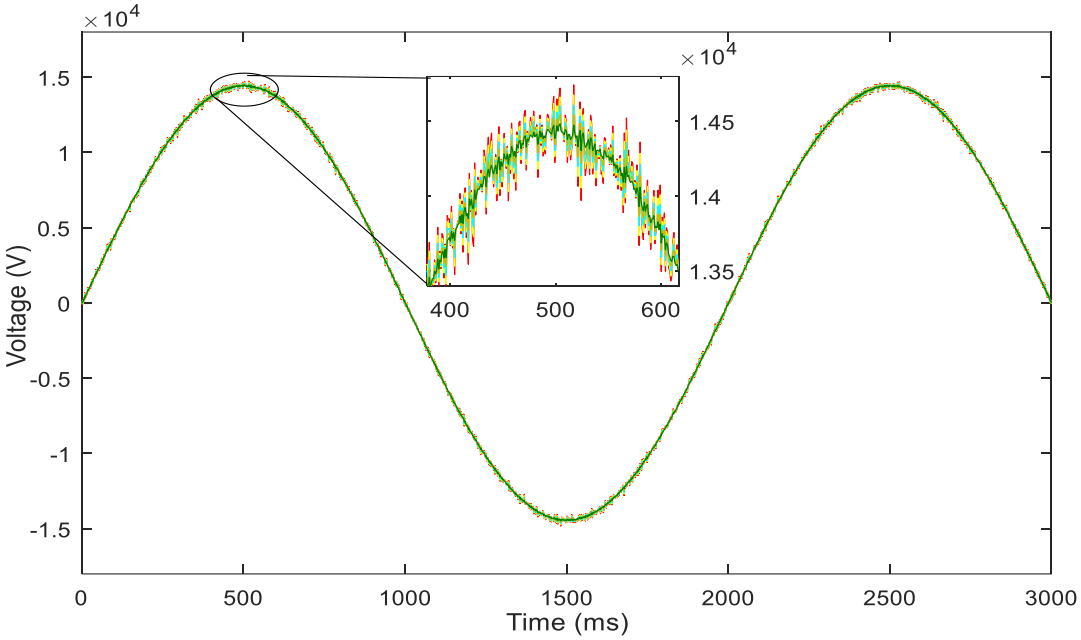

Fig. 4.1 Voltage Signal with Different Noise Levels.

The system considered evaluates a simplistic case where a voltage source at 154 kV rms is connected to a load through a power cable. The output (load) voltage signal is sampled at a specific rate using a zero-order hold device and converted to the frequency domain using the fast Fourier transform (FFT). The PSD of the voltage signal is obtained using the periodogram () function in MATLAB. The use of the periodogram function offered by MATLAB has several variations in terms of syntax. One of them pertains to the use of a window function. The syntax, as presented in [33], is given as

$$[pxx, f] = periodogram(x, window (npts), npts, f_s) \quad (4.1)$$

where ‘pxx’ represents the periodogram power spectral density (PSD) estimate of the input signal, x; ‘window’ represents the type of window function used; ‘npts’ represents

the number of data points and 'f_s' represents the sampling frequency. The absence of a window function can be represented by replacing 'window' with '[]' in Eq. (4.1).

(i) Power spectrum in the absence of windowing

This sub-section focuses on the power spectral density plot obtained for the voltage signal without the use of a window function. The absence of a window function is equivalent to the use of a rectangular window for analysis. The system is modeled in Simulink and load voltage measurements are recorded using a scope block, which displays signals generated during simulation. The data obtained are exported to the MATLAB workspace.

The power spectrum of the output (load) voltage for various noise levels is shown in Fig. 4.2.

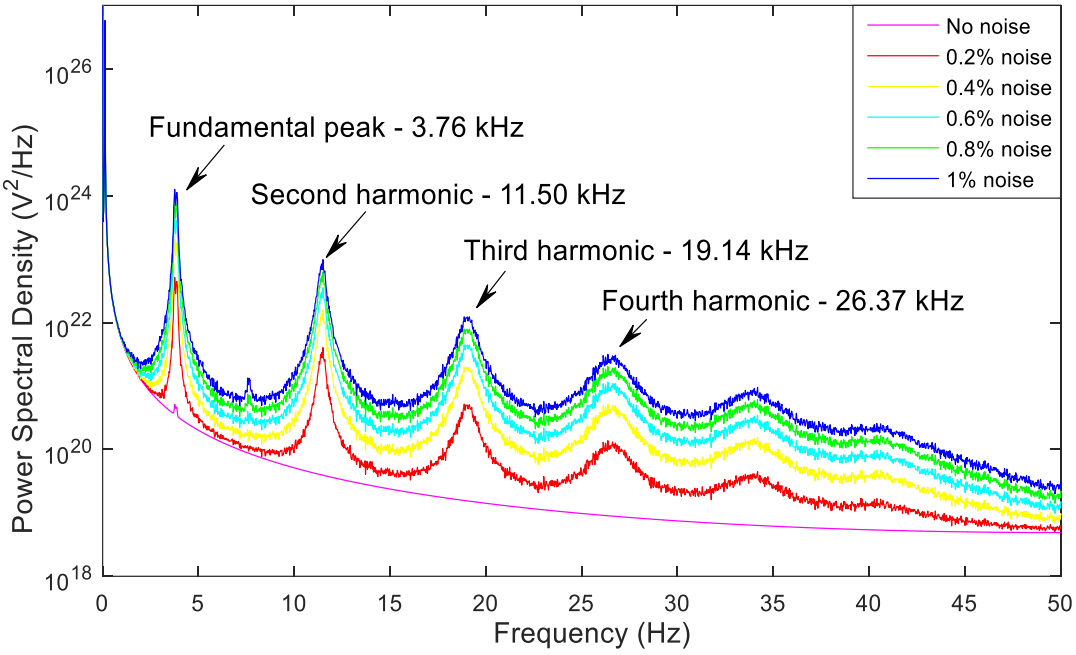

Fig. 4.2 Frequency Spectrums of Load Voltage for Different Noise Magnitudes without a Window Function.

The output voltage signal is sampled at a rate of 10 μs (100 kHz) using a zero-order hold device. The case of having no window is often called or equivalent to the uniform or rectangular window. This is because, even if a window function is not used, the signal is convoluted with a rectangular-shaped window of uniform height [34].

The plot shown in Fig. 4.2 is the result of averaging 100 blocks of data. Each block consists of 2^n data points (n=12 in this thesis) which is a requirement of the FFT algorithm. The percentage of inherent noise in the system determines the amplitude of the resonant peaks but does not affect the actual resonant frequencies. Another observation from Fig. 4.2 is that the lower frequency region has a slight curvature which represents the phenomena of spectral leakage. The next section will show how the effect of spectral leakage can be overcome.

It is observed that higher noise levels in the source lead to a more pronounced appearance of the system resonant frequencies. The resonant frequencies are attenuated and flattened in the high frequency ranges making it more difficult to differentiate them after the fifth harmonic. The fundamental resonant frequency for this case is found to be 3760 Hz ± 12 Hz. The '±' term is concerned with the accuracy of resonant frequency estimation and its origin is explained in Section 4.3. Revisiting the theoretical calculations in Chapter 3, the fundamental frequency calculated using Eq. (3.14) is found to be 3810 Hz. The value obtained from simulation is similar to the theoretical value. The slight variation in values is explained by the fact that the theoretical calculations are performed without considering the load while formulating the transfer function. The second, third and fourth peaks, found from the PSD, occur at 11.50 kHz, 19.14 kHz and 26.37 kHz which are three, five and seven times the fundamental frequency respectively. Thus, the values

obtained through simulation are consistent with the theoretical analysis discussed in Chapter 3.

(ii) Power spectrum in the presence of windowing

For the case of a simplistic system, i.e., only the cable section considered, the effect of windowing has an impact on the power spectrum in terms of the spectral content. The resonant peaks however occur at the same frequencies as in the case of no windowing. The window function used for analysis is the Hann window. The Hann window has the advantage of minimizing spectral leakage and also provides good frequency accuracy which are essential in this case [35]. The power spectrum of the output (load) voltage for various noise levels utilizing the Hann window is shown in Fig. 4.3.

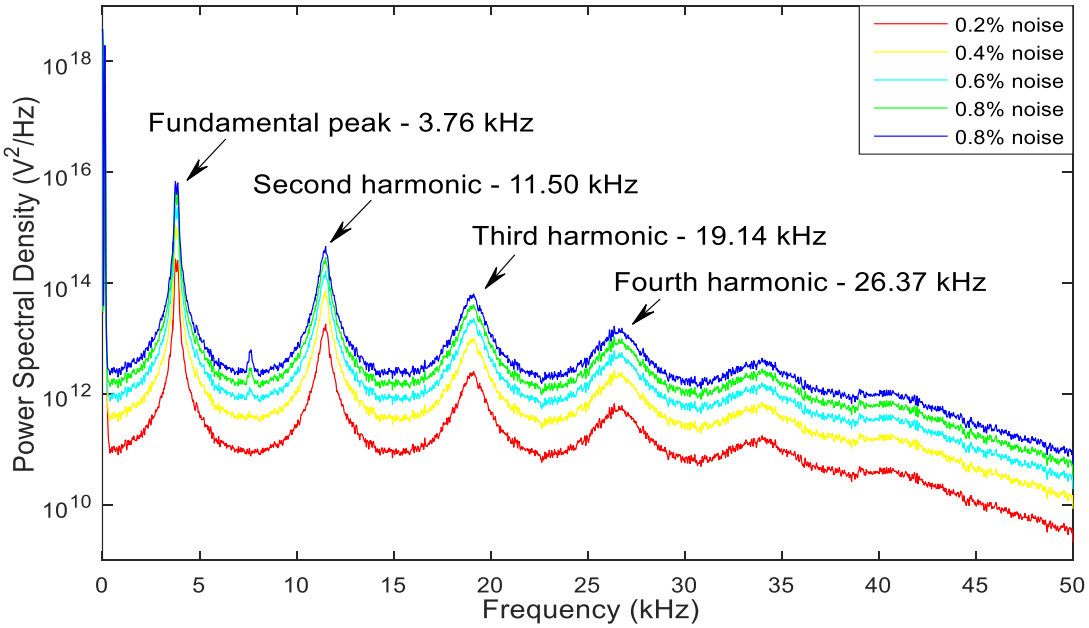

Fig. 4.3 Frequency Spectrums of Load Voltage for Different Noise Magnitudes with a Hann Window Function.

The command and arguments used in MATLAB to obtain the power spectral density are as follows

$$[pxx, f] = periodogram(x, hann(npts), npts, f_s) \quad (4.2)$$

In Eq. (4.2), 'npts' represents the number of data points and is equal to 2^{12} and f_s, the sampling frequency, is the inverse of the sampling time and is equal to 10^5 Hz. From Fig. 4.3, it can be seen that the phenomena of spectral leakage, which Fig. 4.2 exhibited, is eliminated. This is consistent with the fact that the Hann window has less spectral leakage when compared to the no window case which is equivalent to using the rectangular window for analysis. The effectiveness of the Hann window is more evident in the case which considers the transformer connected power system which is discussed in the next section.

4.1.2 Case b : Transmission Line and Transformer

Now that the theoretical analysis for 'Case a' has been successfully verified, the transformer-connected power system is considered for analysis. This case evaluates a more realistic scenario since actual ac power systems have transformers in them. The addition of a transformer changes the impedance of the circuit which is bound to have an effect on the resonant frequencies in the system. A schematic representation of the transformer connected system is shown in Fig. 3.2.

Similar to 'Case a', the system is modeled in Simulink. The source voltage at 10.2 kV (14.428 kV peak to peak) is stepped up to 154 kV which is fed to the power cable. A 116 MVA step-up transformer at the source end with parameters comparable to the actual system is used. The load end of the cable is represented with values which reasonably represent actual system conditions. The load is rated at 100 MVA with a power factor of 0.966. The load voltage is recorded using a scope block, which displays signals generated during simulation.

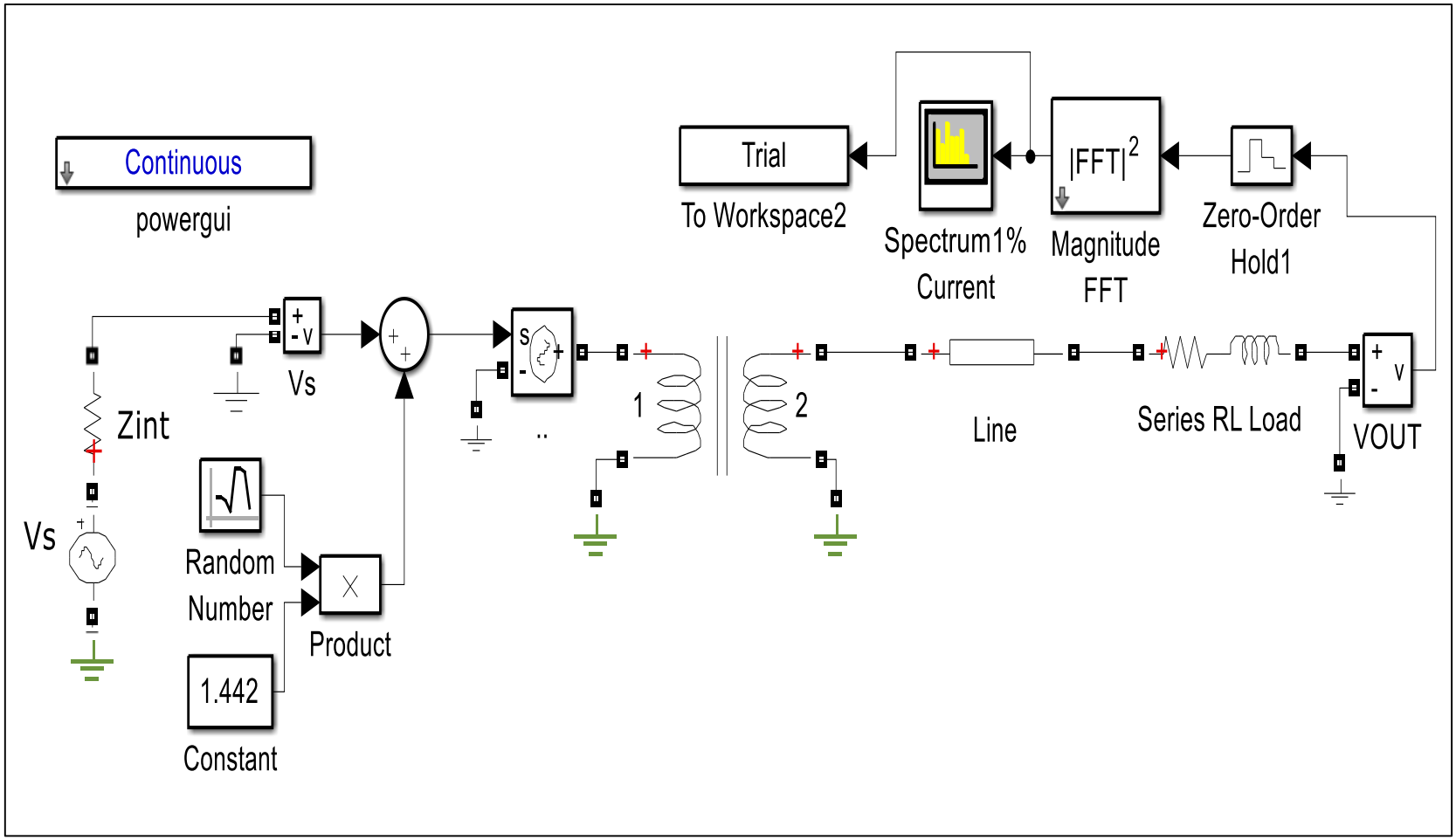

Fig. 4.4 Simulink Model of the Transformer-Connected Power System.

Now, the load voltage is a continuous signal. In order to compute its PSD, it has to be discretized. The discretization is achieved using a zero order hold device which samples the voltage signal at 10 μs (100 kHz). The PSD is then displayed with the help of a spectral analyzer.

The Simulink system model for 'Case b' is shown in Fig. 4.4. The system is simulated under identical conditions as in Case 1 for different noise levels and the voltage signal at the load end of the cable is recorded and analyzed. The results obtained in this case are compared to theoretical calculations presented in Section 3.3.2 to better understand the effect of the transformer on the resonant frequencies.

The load voltage PSD for the transformer-connected system analyzed without a window function is shown in Fig. 4.5.

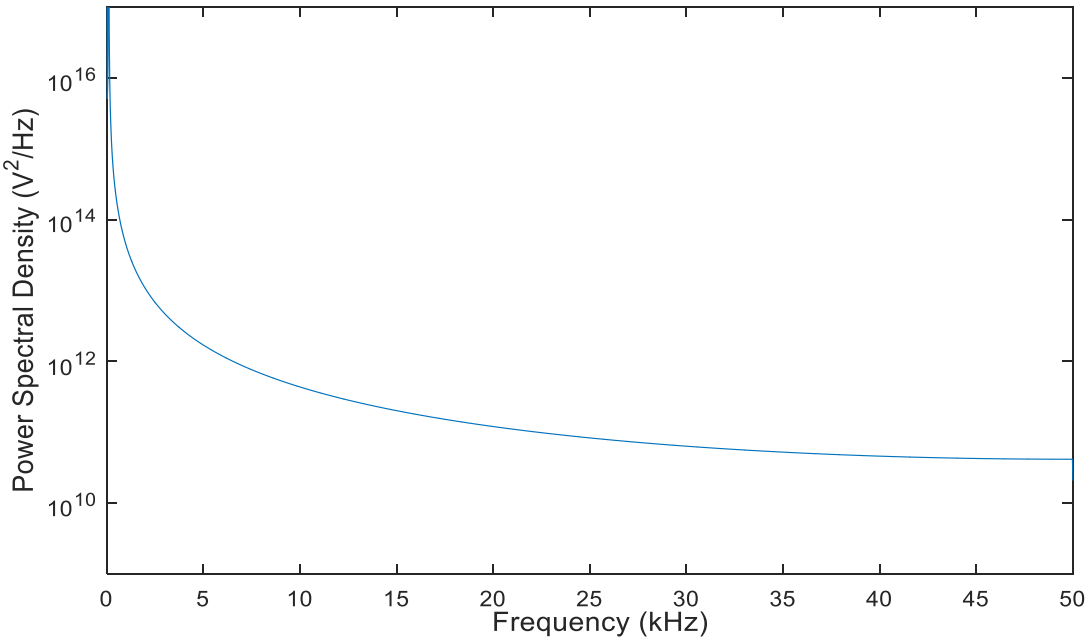

Fig. 4.5 Output Voltage Spectrum without the Window Function for 'Case b.'

It is observed that, in the presence of the transformer, the power spectrum estimate shows no peaks when analyzed without a window function. This is because the analysis of the voltage signal without a window function (which is equivalent to a rectangular window) causes spectral leakage as seen in Fig. 4.2. The effect of spectral leakage can conceal the adjacent resonant peaks.

However, the utilization of the Hann window overcomes this issue and exhibits distinct peaks in the spectrum as shown in Fig. 4.6. This is an important result which demonstrates the importance of a window function in spectral analysis.

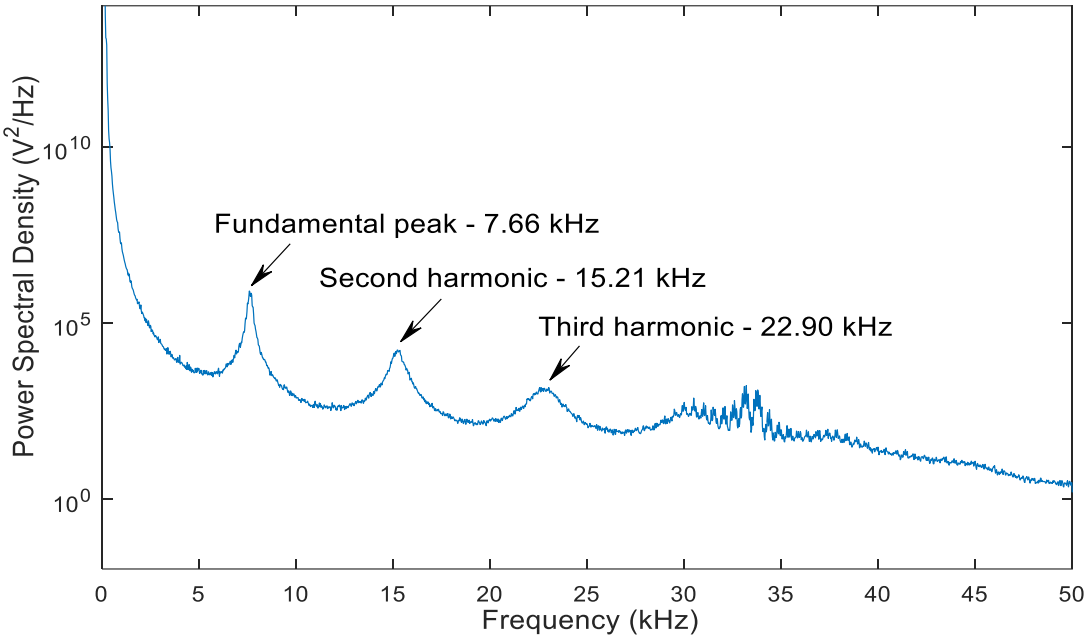

Fig. 4.6 Output Voltage Spectrum with Hann Window Function for 'Case b.'

From Fig. 4.6, it can be seen that the fundamental peak, second and third harmonic occur at 7.66 kHz, 15.21 kHz and 22.90 kHz respectively. According to the theoretical analysis carried out in Section 3.3.2, for the transformer-connected system, the fundamental frequency is found to be twice that of the 3.76 kHz fundamental frequency

for the no transformer case, i.e., 'Case a.' Therefore, the results obtained from simulation are consistent with the theoretical analysis carried out in Chapter 3.

The spectrum obtained using the Hann window function has lower magnitude compared to that without the window function. This can be seen in Fig. 4.7 which compares the load voltage PSD for the transformer-connected system analyzed with and without the window function. This is because the introduction of a window function changes the amplitude of the signal points resulting in a loss in the total energy. In the spectral domain, this loss corresponds to a decrease in the amplitude of the spectra compared to that of the no window case.

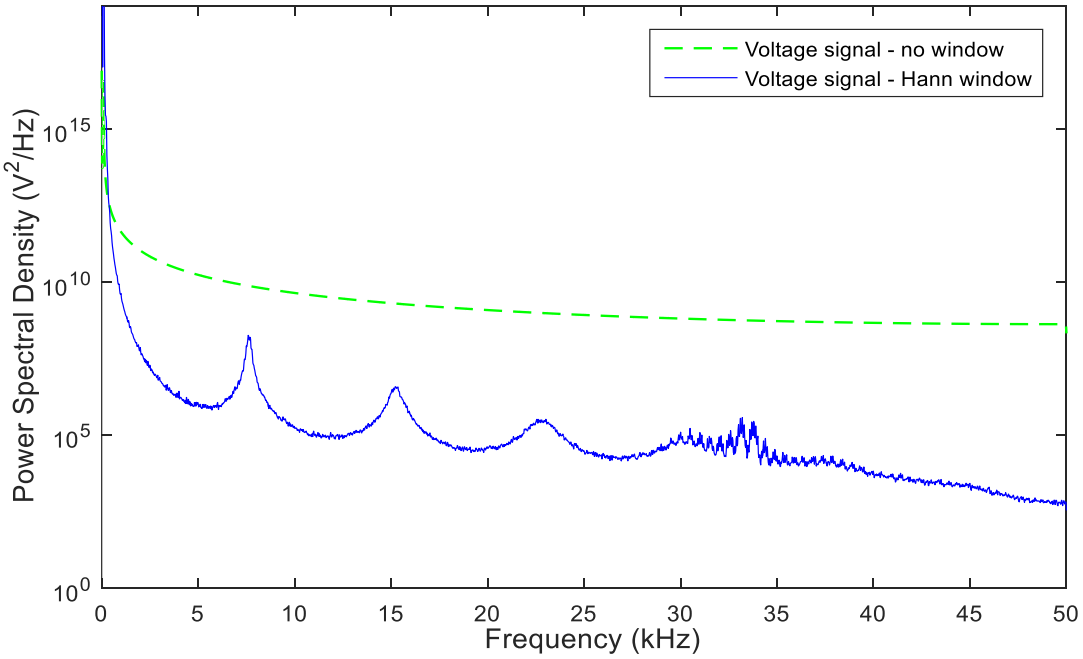

Fig. 4.7 Comparison of Output Voltage Spectra with and Without the Window Function for the Power System with a Transformer and Load.

Another important phenomena observed from the plots is the shift in the resonant frequencies due to the inclusion of a transformer. Consistent with the theory

presented in Section 3.3.2, simulation results also show a shift in the fundamental resonant frequency by a factor of 2. This shift occurs due to the combined effect of the terms in the denominator of Eq. (3.17). The combination of the terms Z_{TR} and $1/Z_c$ reduces the effective inductance of the circuit, thus increasing the resonant frequencies due to their inverse relationship shown in Eq. (3.18). An illustrative comparison of the power spectrums of the voltage signal for 'Cases a and b' is shown in Fig. 4.8. Both cases are analyzed using the Hann window.

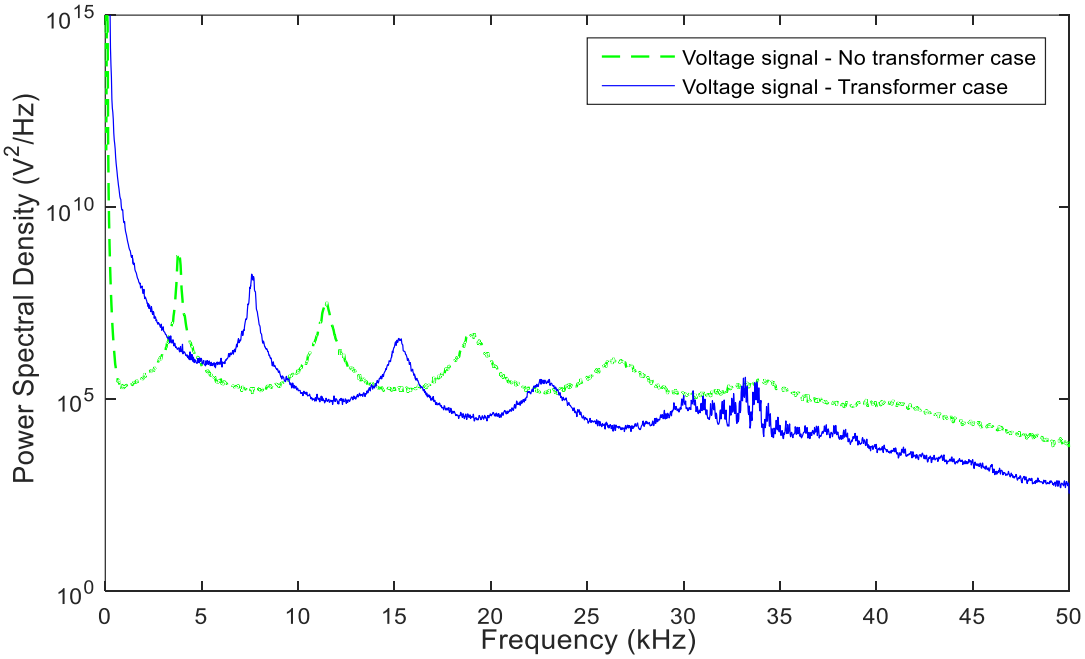

Fig. 4.8 Comparison of Hann-Windowed Output Voltage Spectra with and without Transformer in the System.

The results obtained from simulation are compared for the two cases, i.e., 'Case a' without the transformer and 'Case b' with the transformer in the system. Consistent with theoretical analysis, simulation results also show a shift in the resonant frequencies for the transformer case by a factor of 2. The fundamental resonant peak for the

transformer case occurs at 7660 Hz which is approximately twice the frequency of the system without the transformer, which was found to be 3810 Hz from Fig. 4.3.

The plot for the transformer case is multiplied by a factor of 225. This factor is introduced as a result of the turns ratio of the transformer. The transformer is a step up transformer which has a primary voltage of 10.2 kV and a secondary voltage of 154 kV. Therefore, the turns ratio of the transformer is 15. Since the PSD is being dealt with, which is the square of the magnitude of the FFT, the square of the turns ratio is used as the scaling factor. The scaling is introduced in order to compare the two spectrums due to a difference in the voltage level at the source end for the two cases, i.e., 154 kV for 'Case a' and 10.2 kV for 'Case b.' Table 4-2 compares the resonant peaks for the two cases.

Table 4-2 Comparison of Resonant Frequencies for 'Case a' and 'Case b'

	Resonant Frequency (kHz)	
Cases	'Case a' (No transformer)	'Case b' (Transformer)
Fundamental	3.76	7.66
Second harmonic	11.50	15.21
Third harmonic	19.14	22.90
Fourth Harmonic	26.37	30.25

A similar analysis is now carried out on the current signal. The load current PSD for the transformer system analyzed using the Hann window is shown in Fig. 4.9. The plot in Fig. 4.9 is obtained by sampling the load current at a rate of 10 μs for a noise level of 0.1%.

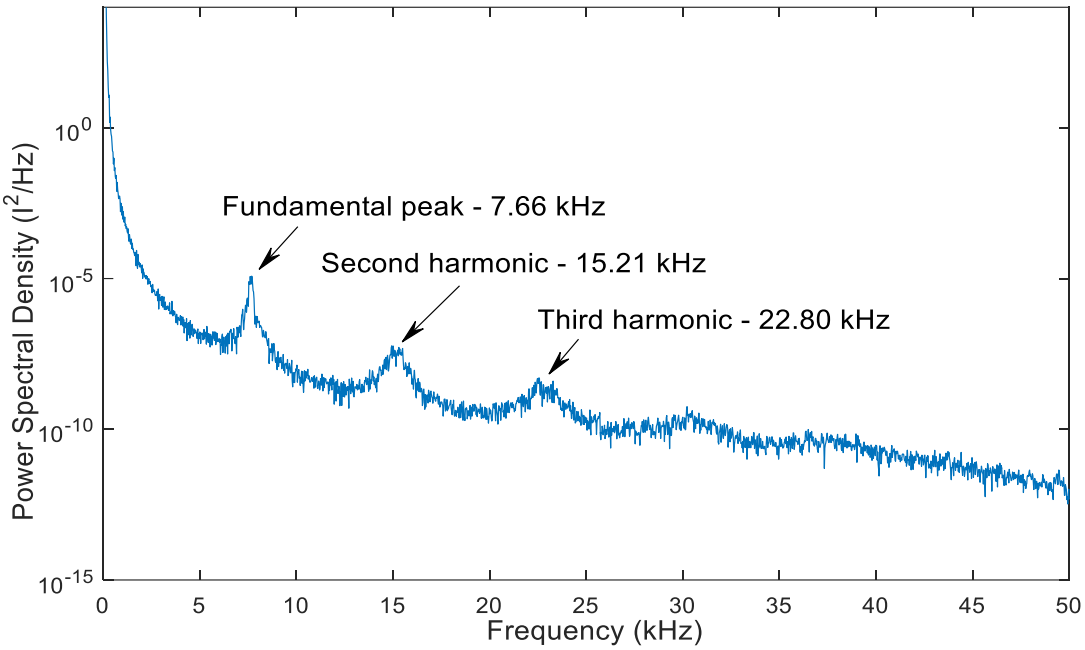

Fig. 4.9 Output Current Spectrum with Hann Window for 'Case b.'

It is observed that, for noise levels below 0.1%, the current signal spectrum does not exhibit distinct resonant peaks. The frequency domain analysis carried out on the current signal is identical to that used for the voltage signal. It is to be noted that the voltage power spectrums shown in Figs. 4.5-4.9 are obtained by simulating the system with an inherent noise level of 0.01%.

4.2 Behavior of Resonant Frequencies in a Faulted Power System

Now that the behavior of the resonant frequencies under normal operating conditions has been studied, the system behavior is analyzed in the presence of a contingency. The contingency considered is a single line to ground fault. The behavior of the resonant frequencies is studied for faults applied at various positions along the length of the cable and for different fault resistance (R_F) values. Different fault resistance values are used to simulate various stages of cable degradation beginning from insulation degradation (high

fault resistance values) to fault conditions (lower fault resistance values). The equivalent circuit for the faulted power system is shown in Fig. 3.5. As mentioned earlier, the cable is 10.5 km long. The point of application of the fault is varied from 5% to 95% of the cable length at increments of 5%, i.e., 0.525 km.

The PSDs of voltage and current signals are recorded for different fault resistance values ranging from 1 mΩ to 1 MΩ and higher. Higher values of fault resistance are simulated in order to evaluate the phenomena of cable insulation degradation. Smaller values of the fault resistance represent the case of a single line to ground fault. It is known that insulation degradation leads to a decrease in cable insulation resistance as a result of which a leakage current flows to ground. Depending on the degree of decrease in insulation resistance, a change in the PSD of the voltage and current signals is observed.

The Simulink model for the faulted case is shown in Fig. 4.10. The transformer block consists of three single-phase transformers rated at 116 MVA, 116 MVA and 58 MVA respectively. Although a three-phase fault block is shown in the figure, only the phase A and ground options are selected to simulate the single line to ground fault on phase A. Based on the simulations performed, the trends in the PSDs of voltage and current signals are observed and conclusions are drawn based on comparisons made with the PSDs obtained from normal operating conditions. The PSDs for the voltage and current signal under normal operating conditions are shown in Figs. 4.6 and 4.9, respectively.

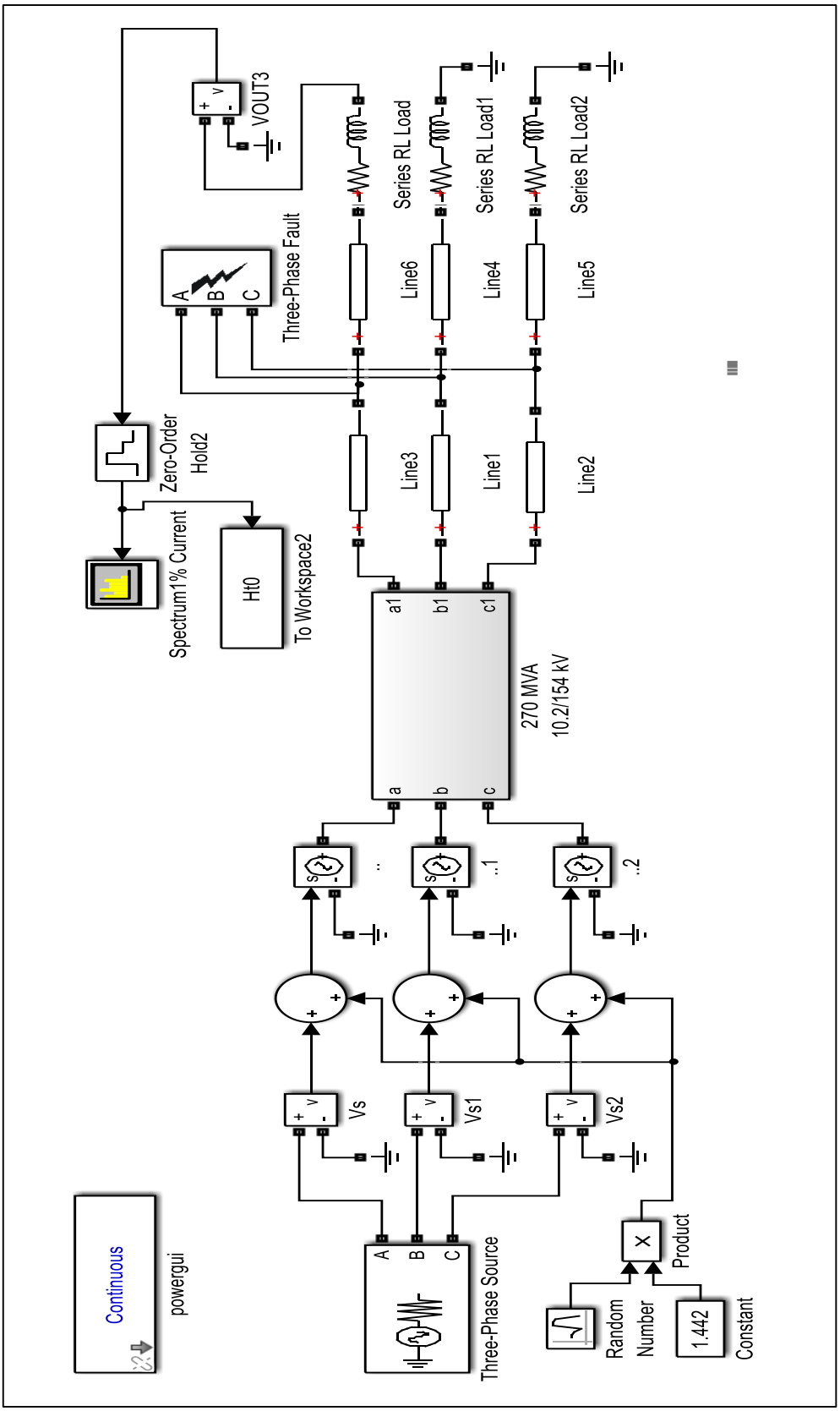

Fig. 4.10 Simulink Model of the Faulted Power System.

The behavior of resonant frequencies for 3 different ranges of fault resistance values are simulated. The first set of values lie between 1 mΩ – 30 Ω, the second between 30 Ω – 1 MΩ and the third for values greater than 1 MΩ. These three cases will be discussed in the next section.

For all three cases, the simulation is run for 1 second with the fault applied at 0.5 seconds. The fault is cleared in 20 ms, at 0.52 seconds. The total number of data points obtained from simulation is 10^5 at a sampling frequency of 100 kHz. The entire data set is not considered for analysis since a significant portion of it represents normal operating conditions. In order to observe the behavior of resonant frequencies under faulted condition, only a small subset of the data points is considered for analysis.

In order to carry out frequency domain analysis, i.e., computing the PSD of the measured signals, a set of data points which most accurately represent the behavior of resonant frequencies under faulted conditions is considered for analysis. The ideal set of data points is decided by trial and error ensuring that the entire fault duration is included. For computing the PSD, the length of each block of data analyzed is set at 2^{12} points, i.e., 4096 points. Hence, the total length of the data set considered for analysis should be a multiple of 2^{12}. The ideal range of time for analysis is fixed from 0.48 s to 0.685 s. This corresponds to 20480 data points which is equivalent to five blocks of data analyzed. This is common for the analysis carried out in the three cases discussed below.

4.2.1 For values of R_F between 1 mΩ – 30 Ω

First, the case of a single line to ground fault on phase A is considered. The value of R_F considered for this case is 1 mΩ. The position of R_F along the cable is varied from 5% to 95% of the cable length in increments of 5%. The simulation settings are

discussed earlier. The data from 0.48 s to 0.685 s are extracted for further analysis. Five blocks of data are averaged with each block having 2^{12} data samples. The PSD for each position is computed using the periodogram function utilizing the Hann window.

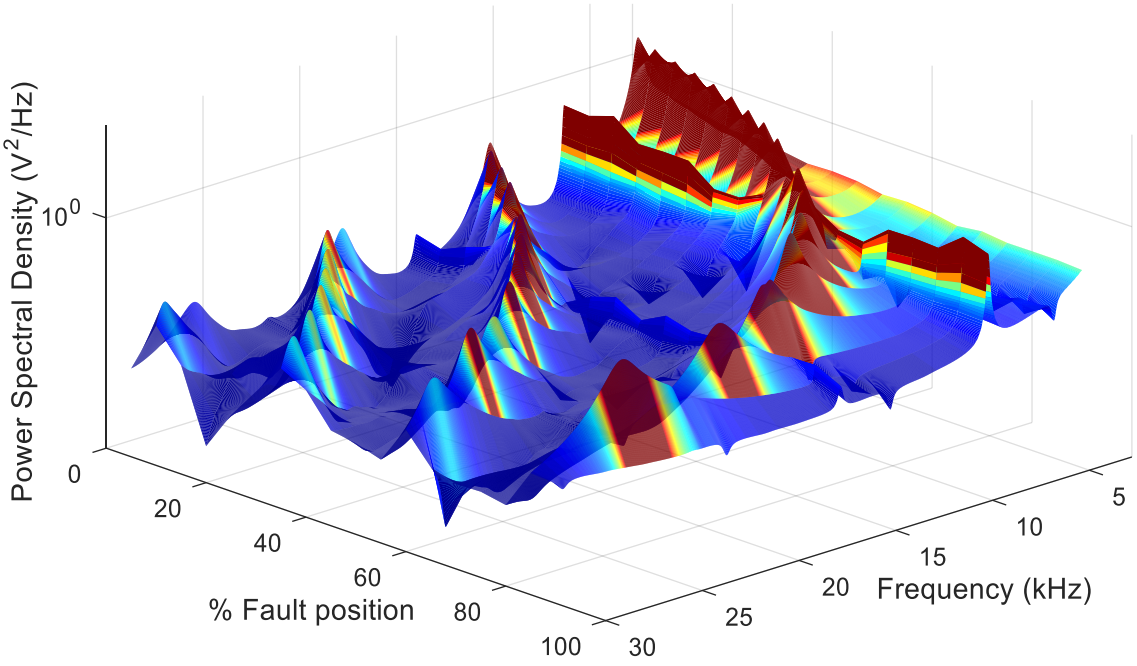

Fig. 4.11 3D Plot of Voltage Signal PSD at Different Fault Locations, R_F = 1 mΩ.

A comparison of the power spectrum for each fault location is shown in the form of a 3D plot in Fig. 4.11. From Fig. 4.11, it can be seen that for every position of the fault resistance along the cable length, a unique set of resonant frequencies appear. Thus, every fault location is uniquely identified based on the frequency at which the fundamental peak and subsequent peaks occur. Table 4-3 provides the resonant frequency values for each fault location. The range of frequencies considered for the analysis carried out is 0–30 kHz. For a fault at the 95% position, the fundamental frequency does not lie in the 0-50 kHz range and hence is not revealed since it lies above the Nyquist frequency.

Table 4-3 Voltage PSD Resonant Peak Frequencies for Different Fault Positions

Fault location (% cable length)	Fault position (km)	Resonant Peak Frequency (kHz)		
		Fundamental	Second	Third
5	0.525	4.004	12.060	20.070
10	1.050	4.248	12.720	21.190
15	1.575	4.492	13.480	22.460
20	2.100	4.761	14.310	23.850
25	2.625	5.078	15.260	25.420
30	3.150	5.444	16.360	27.250
35	3.675	5.859	17.600	29.370
40	4.200	6.348	19.070	31.760
45	4.725	6.934	20.800	34.640
50	5.250	7.642	22.900	38.160
55	5.775	8.472	25.420	42.290
60	6.300	9.546	28.640	47.630
65	8.825	10.890	32.840	-
70	7.350	12.720	38.010	-
75	7.875	15.260	45.830	-
80	8.400	19.040	-	-
85	8.925	25.370	-	-
90	9.450	37.620	-	-

For all the analyses carried out, the region of interest in terms of the frequency range is 0-30 kHz. A similar analysis is carried out on the voltage signal measured at the source end of the cable. The spectrum obtained is found to be a mirror image of the spectrum shown in Fig. 4.11. The presence of these location-specific resonant peaks is observed until a fault resistance value of 30 Ω. For values of R_F greater than or equal to 30 Ω, the behavior of resonant frequencies is discussed in Section 4.2.2.

4.2.2 For values of R_F between 30 Ω – 1 MΩ

This section discusses the behavior of resonant frequencies for fault resistance values greater than or equal to 30 Ω. Fig. 4.12 shows the power spectrum of voltage signals for a fault resistance value of 30 Ω.

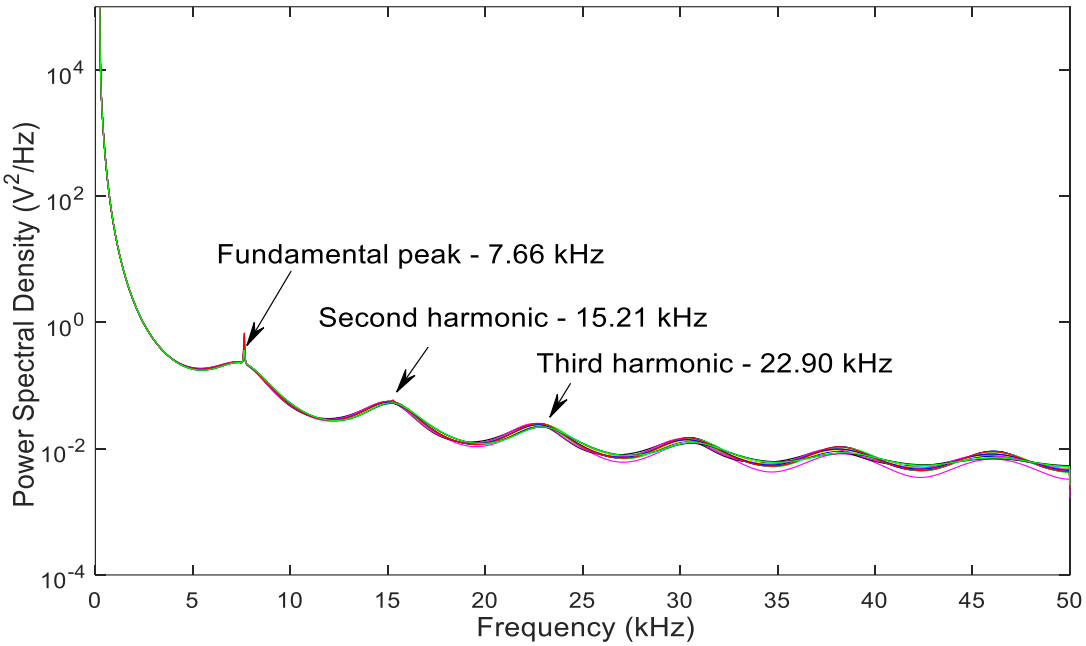

Fig. 4.12 Voltage Signal PSD for Different Fault Locations, R_F = 30 Ω.

It is at this value of R_F that a transition to the fault-free power spectrum is first observed. The value of R_F is increased in 5 Ω increments to evaluate this case. Higher values of R_F lead to a more distinct appearance of resonant peaks as shown in Fig. 4.13.

The idea behind simulating higher values of fault resistance is to verify the fact that, as the cable insulation resistance, which is in the order of thousands of megaohms, is approached, the power spectrum of voltage and current signals should closely resemble the fault-free power spectrums in terms of the frequencies at which the resonant peaks occur. First, the value of R_F for which the resonant peaks show a transition from the

faulted case to the fault-free case is determined. This value is found to be 30 Ω. The representative value of R_F presented in Fig. 4.13 is 100 Ω.

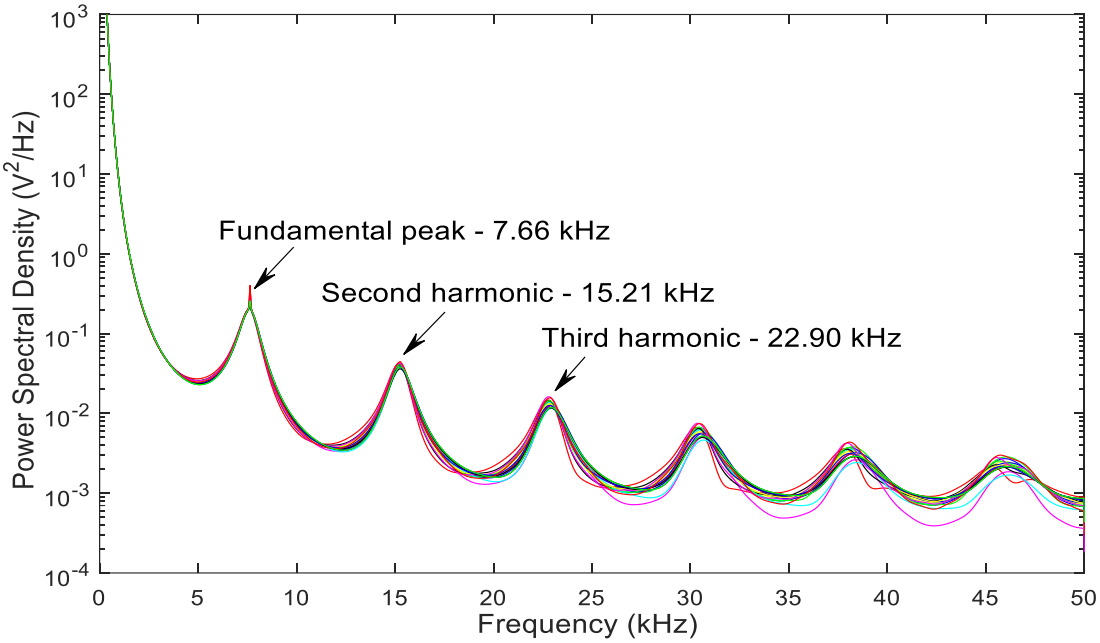

Fig. 4.13 Voltage Signal PSD for Different Fault Locations, R_F = 100 Ω.

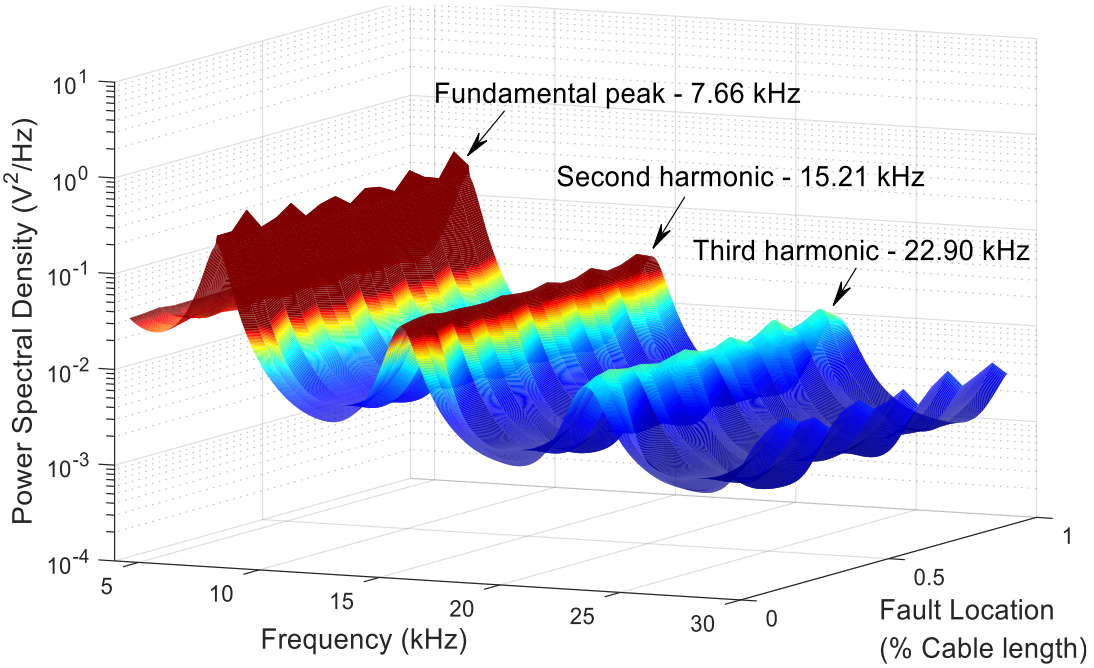

Fig. 4.14 3D Plot of Voltage Signal PSD at Different Fault Locations, R_F = 100 Ω.

4.2.3 For values of $R_F \geq 1$ MΩ

This section discusses the behavior of resonant peaks for fault resistance values of 1 MΩ and greater. Typically, for cables rated in the 100 kV range, insulation resistance values are in the order of thousands of megaohms. As mentioned earlier, based on theoretical knowledge, it can be said that the position of the resonant peaks in the power spectrum should resemble the fault-free condition as R_F approaches the cable insulation resistance value.

In order to validate this premise, the system is simulated for a fault resistance value of 1 MΩ and the power spectrum of the voltage signal is computed.

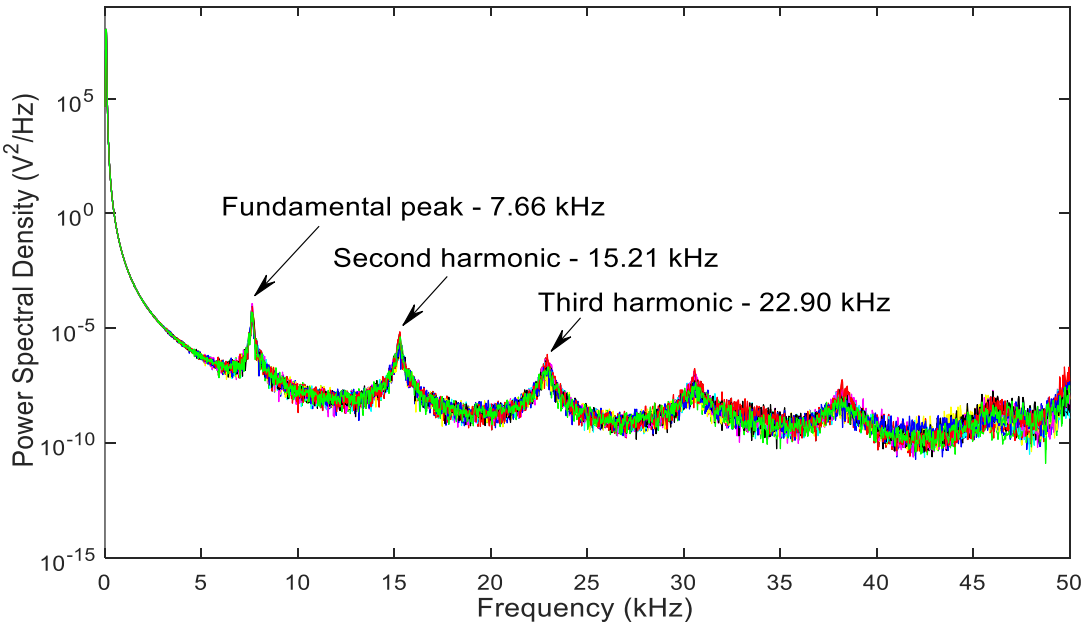

Fig. 4.15 Voltage Signal PSD for Different Fault Locations, R_F = 1 MΩ.

Based on the plots shown in Figs. 4.15 and 4.16, it can be seen that the frequencies at which the resonant peaks occur are identical to the fault-free case for all values of R_F in this range.This verifies the theoretical explanation mentioned earlier

regarding cable insulation resistance. Higher fault resistance values can also be interpreted as a condition similar to insulation degradation in cables, which can be considered as the early stages of a faulted condition.

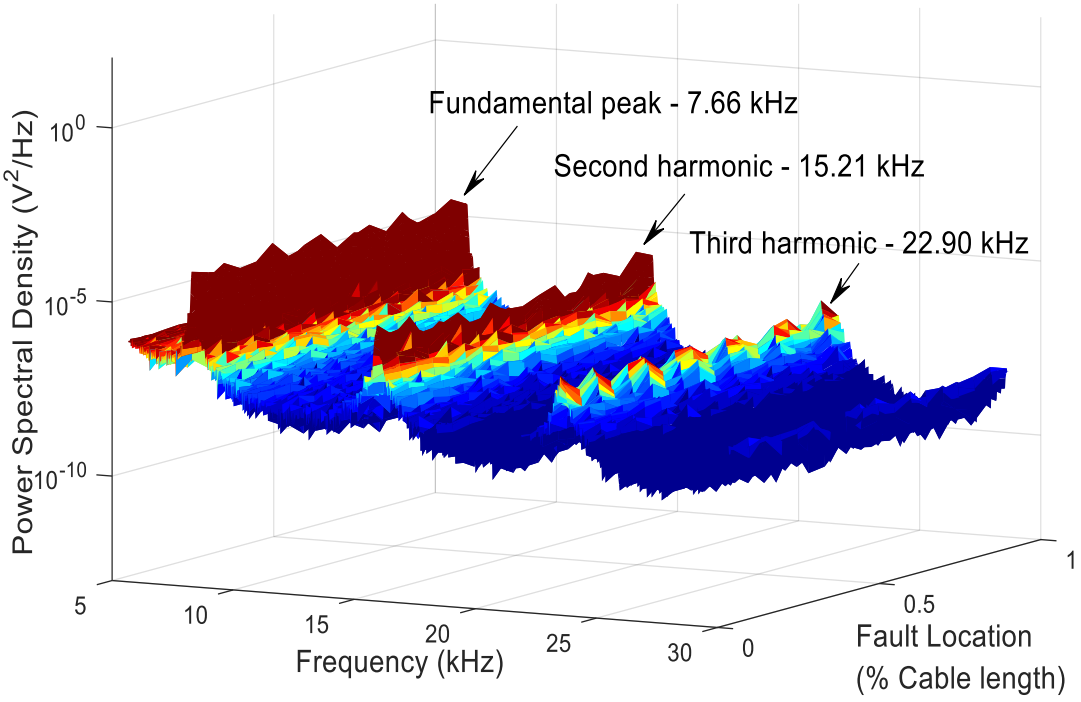

Fig. 4.16 3D Plot of Voltage PSD for Different Fault Locations, R_F = 1 MΩ.

4.3 Analysis of Resonant Frequency Behavior in a Faulted Power System

Sections 4.1 and 4.2 presented the behavior of resonant frequencies under normal and faulted conditions based on computer simulations. Considering the faulted power system case discussed in Section 4.2.1, for the different fault positions simulated, an analysis on the spectrums obtained for each position is carried out.

Fig. 4.17 shows the trend followed by the peaks for the two different cases. The vertical lines represent the frequencies at which the fundamental, second, third, fourth and fifth harmonics appear for the fault-free case. Whereas, the curved lines represent the

position of the fundamental, second and third harmonics for a single line to ground fault case (R_F = 1 mΩ).

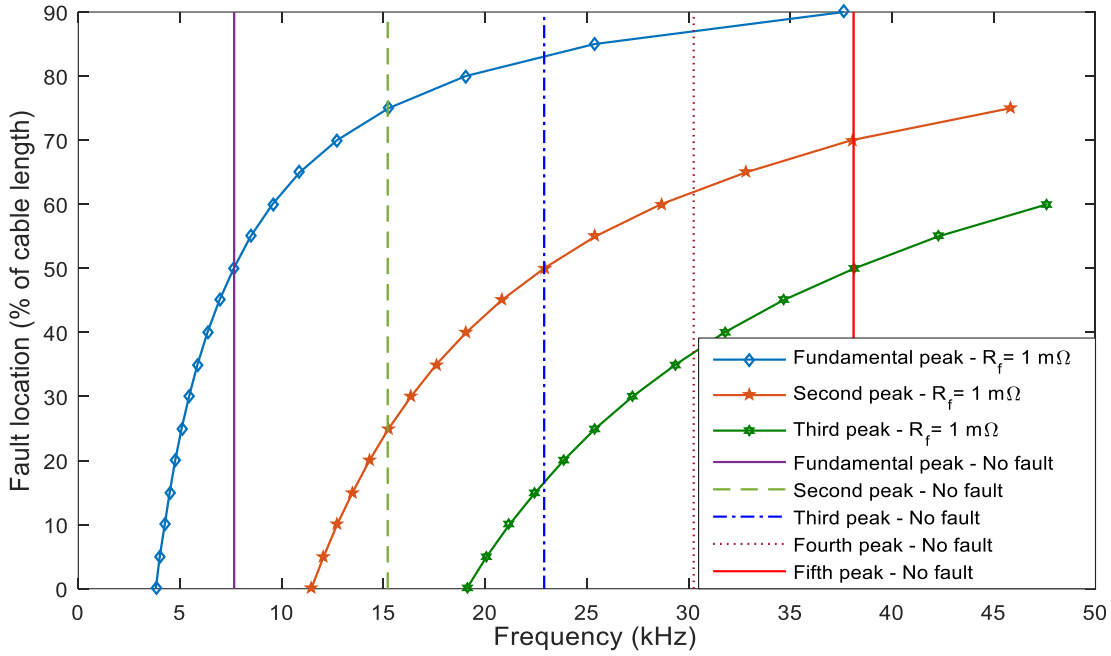

Fig. 4.17 Comparison of Resonant Frequencies for Fault-free and Fault Cases – Load Voltage.

The frequencies at which these peaks occur are unique for each fault location and hence provide an accurate estimate of the fault location. The plot shown in Fig. 4.17 is obtained based on the values presented in Table 4-3.

From Fig. 4.17, it can be observed that, when the fault occurs at the halfway point (50% length of the cable), the fundamental, second and third harmonics of the faulted curves intersect the odd harmonics of the fault-free lines. Since the fundamental frequencies for both faulted and fault-free cases are identical, a fault occurring at the 50% point should be identified by observing higher order, i.e., second and third order resonant frequencies.

Another observation from Fig. 4.17 is that the slope of the three curves is steep for faults occurring before the 50% mark and decreases gradually as the fault position is increased past the 50% point. Thus, the accuracy of predicting cable fault location will be higher for positions beyond the 50% mark compared to those prior to the halfway point. However, earlier in Section 4.2.1, it was stated that the PSD of the source end voltage is found to be a mirror image of the load end voltage PSD. This phenomena is shown in Fig. 4.18.

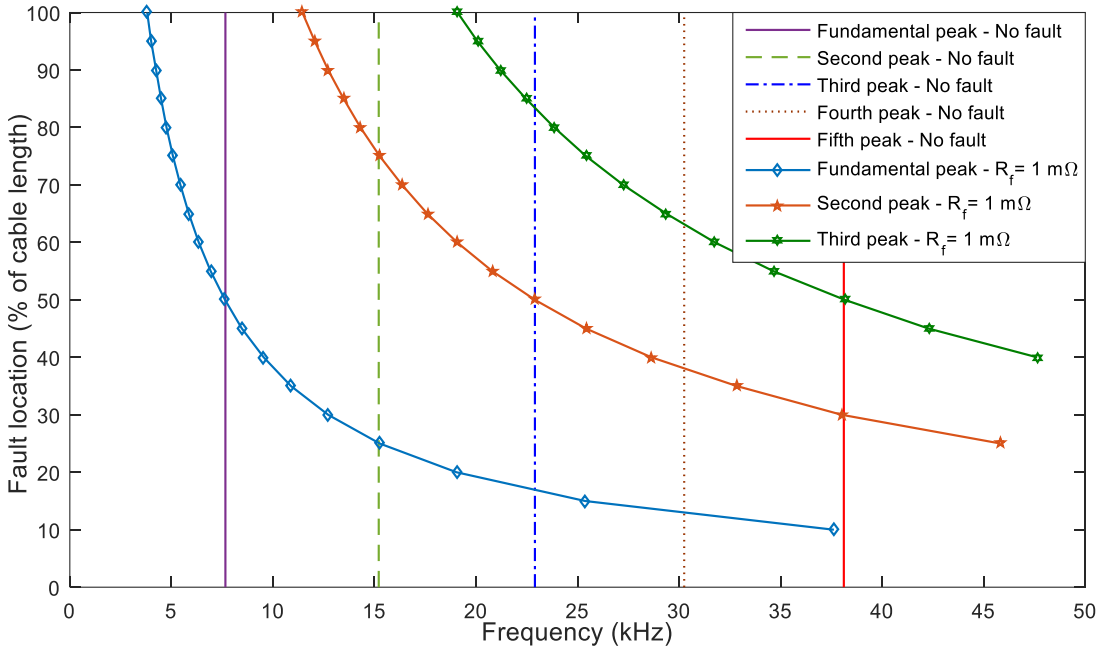

Fig. 4.18 Comparison of Resonant Frequencies for Fault-Free and Fault Cases – Source Voltage.

From Fig. 4.18 it can be seen that the slope of the curve is steep for fault positions beyond the halfway point and small for fault positions before 50% of the cable length. Therefore, making use of both the source end and load end voltage spectrums improves the accuracy of predicting fault location.

Earlier, in Section 4.2.1, it was mentioned that estimating faults at the 95% point cannot be achieved through load end measurements as the fundamental frequency is greater than the Nyquist frequency. However, since the source end measurement spectrum is found to be a mirror image of the load end case, faults at the 95% point can be predicted as illustrated in Fig. 4.18. Alternatively, a higher sampling frequency could be used which would correspondingly increase the Nyquist frequency. Another important point to be kept in mind is the point of measurement of system signals. As seen from Figs. 4.17 and 4.18, the point of measurement affects the manner in which resonant frequencies for a particular fault position are interpreted.

The accuracy of estimating the fault location depends on the frequencies (f_r) at which the resonant peaks occur, the sampling frequency (f_s) and the number of data points (*npts*) considered while computing the PSD. Consider the frequency at which a peak is measured to be 'f'. In reality, the peak can be anywhere in the range of $f \pm (\Delta f/2)$. The value of Δf depends on the sampling frequency and number of data points per block.

In this case,

$$f_s = 100 \text{ kHz}, \qquad npts = 2^{12} = 4096$$

$$\Delta f = \frac{f_s}{npts} = \frac{100{,}000}{4096} = 24.4 \text{ Hz} \qquad \ldots (4.3)$$

$$f_r = f \pm \left(\frac{\Delta f}{2}\right) = (f \pm 12) \text{ kHz} \qquad \ldots (4.4)$$

Now, consider the case of a fault occurring at 50% cable length. The fundamental frequency for this case is 7.642 kHz. From Eqs. (4.3) and (4.4), the actual frequency range for this peak can lie anywhere in between 7.630 kHz and 7.654 kHz. The corresponding fault location values for the above frequencies from Fig. 4.17 are 5.240 km to 5.2584 km.

Thus, the accuracy of fault location can be estimated to an 18.4 m range. For faults occurring at 70% cable length and higher, the accuracy is further improved to a 6.7 m range. Looking at the fault curves in Figs. 4.17 and 4.18, it can be said that the accuracy of locating faults will be higher for those occurring the far end (load end) of the cable for load end measurements and near end (source end) of the cable for source end measurements.

Chapter 4 dealt with verifying the theoretical analysis and also discussed the behavior of resonant frequencies under faulted conditions based on computer simulations. Chapter 5 will deal with the analysis of actual power system data and its comparison with the simulation results presented in Chapter 4.

CHAPTER 5

ANALYSIS OF ACTUAL SYSTEM DATA

The validity of any theory and simulation depends on how well they compare with actual system conditions. The results obtained from the simulations in Chapter 4 are compared with measured data from a power system. This involves frequency analysis of system data and comparison of power spectrums of the measured data and simulation data.

5.1 Actual System Voltage and Current Data

Before analyzing actual system data in the frequency domain, the voltage and current signals measured from an actual power system are observed with respect to time. The measured data are obtained from a renewable energy installation located in South Korea. Figs. 5.1 and 5.2 present snapshots of the voltage and current signals measured from the actual system. The data are measured for a total time duration of 4 seconds and sampled at 2 μs intervals (500 kHz).

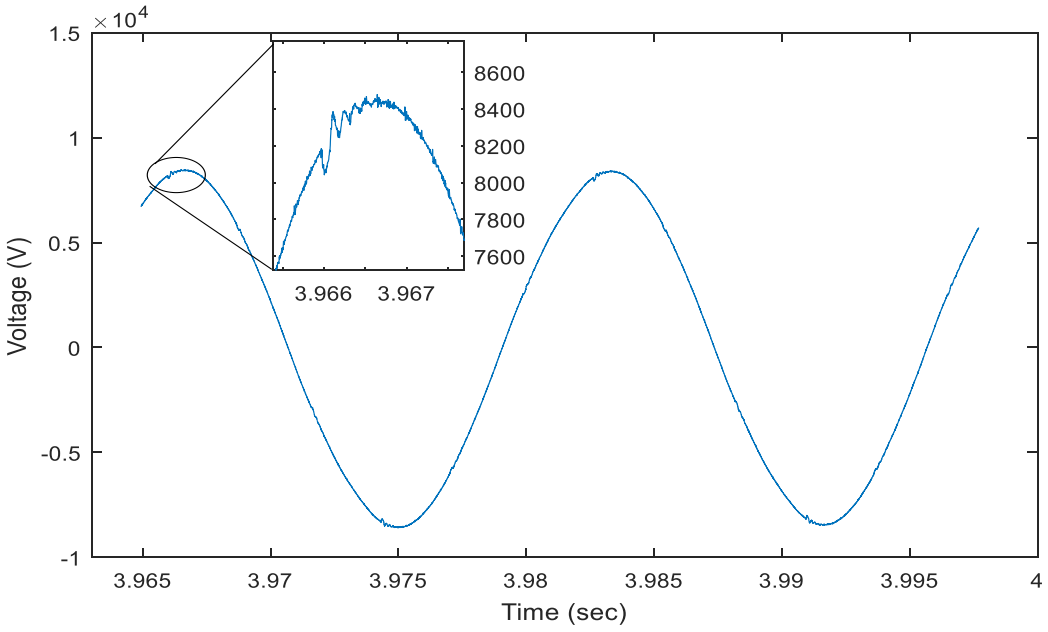

Fig. 5.1 Measured Voltage from the Actual Power System.

The data provided for analysis are split into smaller data sets for the convenience of analysis. The total number of data samples is $2x10^6$. The number of data points per block considered for analysis is 2^{14}. The entire data set is thus split into 122 blocks with 2^{14} data points per block. Figs. 5.1 and 5.2 represent one such block of data. The value for the number of data points per block is chosen such that at least 2 cycles of the signals are included.

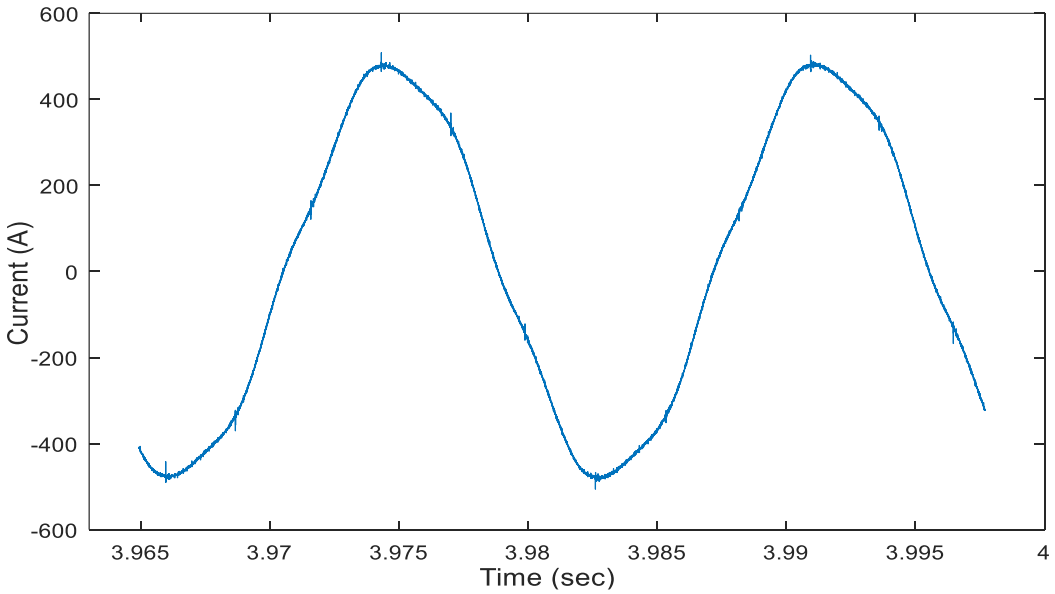

Fig. 5.2 Measured Current from the Actual Power System.

From Figs. 5.1 and 5.2, it can be seen that the voltage signal represents a pure sinusoidal function with some inherent noise observed from the minute fluctuations in the signal. However, the current signal shows some distortion and does not represent a pure sinusoidal function. The total harmonic distortion and inherent noise level in the voltage and current signals are computed in the subsequent sections. Due to distortions in the current signal, it is not considered for comparison with the simulated data due to possibility of inaccuracies in the power spectrum estimate when compared to the voltage

signal. Hence, the primary focus is on observing how well the actual voltage signal compares to the simulated data.

5.1.1 Total Harmonic Distortion

Typically, the quality of the voltage and current signals is determined by a factor called total harmonic distortion (THD). Total Harmonic Distortion is defined as "the ratio of the root mean square of the harmonic content, considering harmonic components up to the 50th order and specifically excluding interharmonics, expressed as a percent of the fundamental. Harmonic components of order greater than 50 may be included when necessary" [36]. Every waveform has some harmonic distortion associated with it. In the case of an ac signal, the smaller the THD, the closer the waveform resembles a pure sinusoid. The IEEE Recommended Practice and Requirements for Harmonic Control in Electric Power Systems (IEEE standard 519-2014) sets limits on voltage and current harmonics. Typically, recommended practices such as IEEE-519, IEEE-1547 stipulate that a current with THD greater than 5% cannot be injected into the grid by any distributed generation source [37]. Table 5-1 shows the recommended limits for harmonic distortion in voltage signals.

Table 5-1 Voltage Distortion Limits [36]

Bus voltage V at Point of Common Coupling	Individual harmonic (%)	Total harmonic distortion THD (%)
$V \leq 1.0$ kV	5.0	8.0
1 kV < $V \leq 69$ kV	3.0	5.0
69 kV < $V \leq 161$ kV	1.5	2.5
161 kV < V	1.0	1.5

Even though the current signal is not considered for analysis, its THD is computed. The THDs of actual system voltage and current signals are calculated in MATLAB. The syntax, as presented in [38], is given as

$$r=thd(x,fs,n) \quad \ldots (5.1)$$

where ‘r’ represents the total harmonic distortion in dBc specified as a real value scalar; ‘x’ represents a real-valued sinusoidal input signal specified as a row or column vector; ‘fs’ represents the sampling frequency, specified as a positive scalar and ‘n’ represents the number of harmonics as a positive integer.

For the actual system data, sampled at 500 kHz, the THDs of the voltage and current signal are found to be -38.1609 dBc and -26.3299 dBc respectively. In terms of percentage, the THDs of the voltage and current signal are 1.24% and 4.83%, respectively, which lie within the prescribed IEEE standard.

5.1.2 Inherent Noise Level

While computing the THD of the voltage and current signal, only the harmonics, i.e., multiples of the 60 Hz frequency, are considered in the analysis. However, in order to estimate the noise level in the signal, every frequency except for the 60 Hz fundamental frequency is taken into consideration. The noise level is estimated by integrating the area under the power spectrum using the ‘bandpower’ function in MATLAB. The syntax, as presented in [39], is given as

$$p = bandpower(Pxx,Fs,freqrange,'psd') \quad \ldots (5.2)$$

where ‘p’ returns the average power contained in the frequency interval, freqrange; ‘Pxx’ represents the power spectral density estimate of the signal and ‘Fs’ is the sampling frequency.

Now, in order to compute the noise level, the power spectrum is divided into three frequency ranges as described below

f_{left} : 0 – 59.7 kHz

$f_{fundamental}$: 59.8 – 60.25 kHz

f_{right} : 60.26 – 250 kHz

Since the data are sampled at 500 kHz, the Nyquist frequency is 250 kHz in this case. Using the syntax shown in Eq. (5.2), the average power for each of the above frequency ranges is calculated. The percentage noise levels in the voltage and current signal are obtained by taking the ratio of the average power for all frequencies ranges except the fundamental frequency range to the average power of the fundamental frequency range. This is better explained in Table 5-2 using numerical data obtained from MATLAB analysis of the actual measured signals.

Table 5-2 Average Power and Noise Level Data

Signal	Average power (V^2/Hz, I^2/Hz)		
	Fundamental range $P(f_{fundamental})$	Noise $P(f_{left} + f_{right})$	% Noise
Voltage	3.5322e+07	2.7053e+04	0.0765
Current	9.7755e+04	466.5794	0.4751

Based on the values presented in Table 5-2, the percentage noise levels in the voltage and current signal are found to be 0.0765 % and 0.4751 %, respectively. This is consistent with the fact that Fig. 5.2 shows that the current signal has a higher percentage of noise and harmonic distortion when compared to the voltage signal in Fig. 5.1.

5.2 Deciding the Optimum Parameters for Frequency Analysis

Frequency domain analysis of the actual data is carried out by computing its power spectral density. This is carried out by utilizing the periodogram function in MATLAB. The syntax for using the periodogram function is expressed in Eq. (4.1). The two important parameters that have to be chosen in order to perform accurate analysis are the window function type and the number of data points, npts.

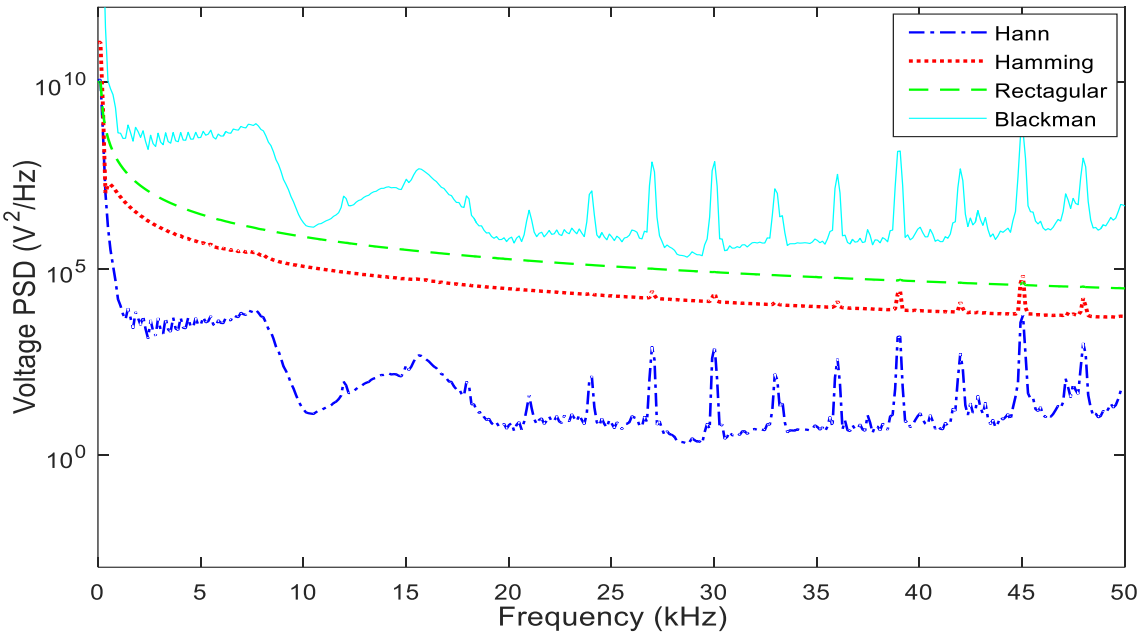

Fig. 5.3 Actual Voltage Spectrum using Different Window Functions (Npts=2^{12}).

In order to find out which combination of window function and data points can be chosen, the actual data set is analyzed with different window functions and data points and the results obtained from each of them are compared. From Fig. 5.3, it can be seen that the rectangular window and Hamming window are ineffective and hence cannot be used. The Hann window and Blackman window however, show identical results.

The curves in Fig. 5.3 are multiplied by a scaling factor to prevent overlap. Out of the two window functions, the Hann window is chosen for further analysis since it has better frequency resolution and lesser leakage [35]. Also, the Blackman window has a wider main lobe and higher side lobe attenuation compared to the Hann window and hence not preferred over the Hann window [40].

Now that the appropriate window function has been chosen, the number of data points to be analyzed is decided. Fig. 5.4 shows the power spectrums for different numbers of data points analyzed per block utilizing the Hann Window. From Fig. 5.4, using 2^{14} or 2^{13} data points does not seem ideal due to the presence of relatively large fluctuations in the low and high frequency regions.

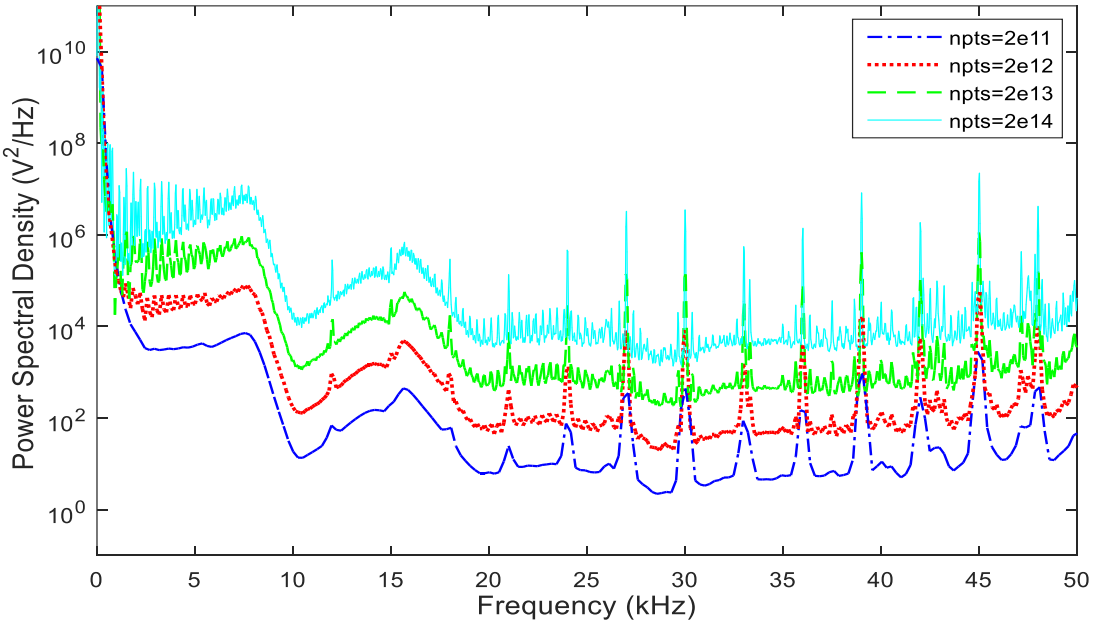

Fig. 5.4 Actual Voltage Spectrum for Different 'npts' using Hann Window.

Now, the tradeoff involved while choosing the number of data points is that a higher number of data points provides a finer frequency resolution but leads to analyzing fewer

blocks of data, thus reducing PSD accuracy. Therefore, a reasonable choice for the number of data points would be 2^{12}.

5.3 Frequency Analysis of Actual System Data

Now that the appropriate choice of the window function and the number of data points to be analyzed is made, the actual system data are analyzed. The measured data are obtained from a renewable energy installation located in South Korea. The cable under consideration is the 154 kV, 10.5 km long XLPE cable described in Section 4.1. The data obtained from the system are measured at a point after the voltage is stepped up after the generator. The data are sampled at 500 kHz for a period of 4 seconds. The measured voltage and current data from the system are analyzed in MATLAB using frequency domain analysis techniques. The Fast Fourier Transforms (FFT) of the voltage and current data are computed and their power spectral densities are obtained, shown in Figs. 5.5 and 5.6.

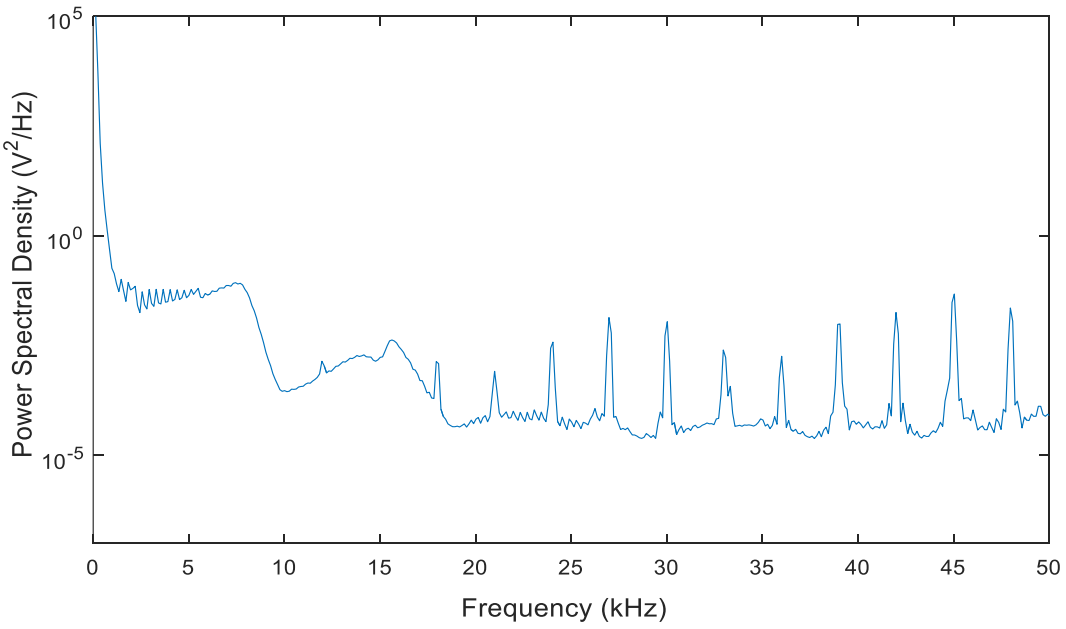

Fig. 5.5 Power Spectrum of Actual System Voltage at the Measurement Point.

An initial look at the voltage signal spectrum in Fig. 5.5 shows several distinct peaks. However, the peaks of interest here are the fundamental and second resonant peaks which occur at 7.69 kHz and 15. 63 kHz respectively. By visual inspection, it is observed that these peaks occur at frequencies close to those observed in the simulated results shown in Fig. 4.6.

Looking at Fig. 5.5, the low frequency region shows some fluctuations and the high frequency region shows sharp peaks. Since the data obtained are from a renewable energy installation, the presence of power electronic switching circuits can contribute to the fluctuations and sharp peaks observed in the low and high frequency region of the power spectrum respectively. Another notable observation is that the position of the two significant peaks are relatively close to those in the simulated case discussed in Section 4.1.2. This also confirms the fact that the voltage measurement point in the actual system is after the step up transformer.

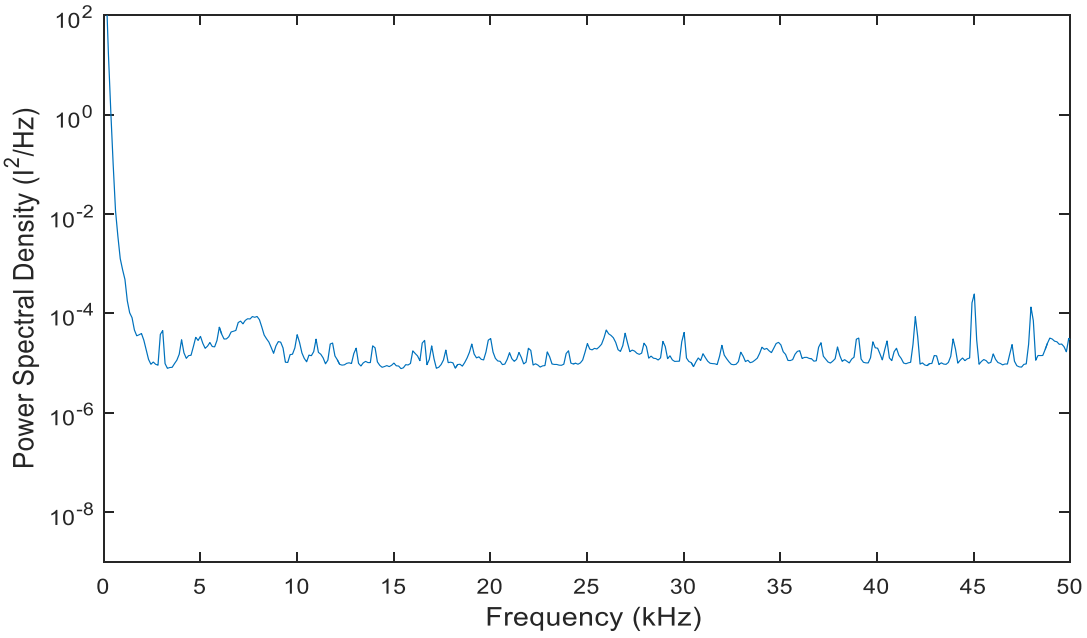

Fig. 5.6 Power Spectrum of Actual System Current at the Measurement Point.

For the current signal, the power spectrum is shown in Fig. 5.6. It can be seen that, compared to the voltage signal spectrum, the current signal spectrum shown in Fig. 5.6 shows only the fundamental peak at 7.69 kHz. Compared to Fig. 4.9 which shows the power spectrum of the current signal from the simulated system, the actual system current spectrum does not serve as a good means of comparison due to the absence of distinct resonant peaks.

A more detailed comparison of simulated data and actual system data is discussed in the next section.

5.4 Comparison of Actual System Data with Simulation and Analytical Results

A comparison of spectrums for measured and simulation data is shown in Fig. 5.7.

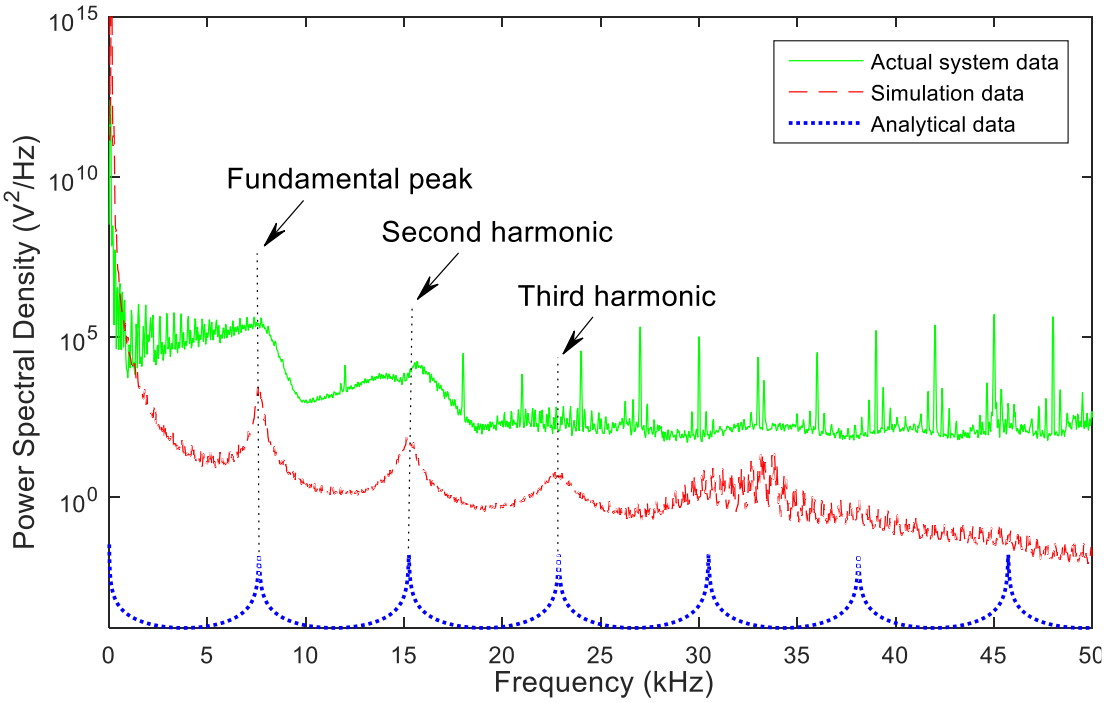

Fig. 5.7 Comparison of Actual System and Simulated Data Spectra.

The simulation data spectra shown in Fig. 5.7 represents the power spectrum of the system modeled with 0.01% normally distributed random fluctuations, i.e., the magnitude of random fluctuations is 0.01% of 14.42 kV (peak-to-peak source voltage) which is 1.442 V injected at the source. The system is simulated under this condition and the spectrum of the voltage signal after it is stepped up is obtained using FFT analysis. A higher noise level changes the amplitude of the curve but does affect the resonant frequencies in the system. The curves represented in Fig. 5.7 are scaled for the ease of comparison.

A comparison of the spectra based on the frequencies at which the resonant peaks occurs for three different cases is shown in Table 5-3.

Table 5-3 Interpretation of Actual System Measurement and Simulation Data Spectra

Resonant Peak	Frequency (kHz)		
	Analytical Data	Simulation Data	Actual System Data
1	7.62	7.66	7.69
2	15.24	15.21	15.63
3	22.86	22.90	-
4	30.49	-	-
5	38.11	-	-

It is observed that the results obtained from simulation and analytical computation are comparable to the actual system data spectrum. It is to be noted that the values obtained through analytical analysis do not consider the load in the system. Also, the simulation data are obtained based on an approximate representation of the actual power system in terms of system components and any external connections. This explains the slight variation in the resonant frequencies of the three cases presented in Table 5-3.

CHAPTER 6

CONCLUSION AND FUTURE WORK

This thesis investigates a novel online monitoring and fault location methodology for underground power cables based on observing the power spectral densities of electrical signals. The term ‘online’ is used since the cable can continue to be connected to the system while its condition is monitored. The presence of inherent fluctuations in a power system, though undesirable, is a key requirement for this methodology. The proposed methodology takes advantage of these inherent fluctuations to elicit the behavior of resonant frequencies under normal and anomalous conditions as well as to accurately estimate fault location.

This thesis begins with introducing existing methodologies for cable monitoring and diagnosis. A review of online and offline methods for cable fault detection is also presented. This is followed by establishing a theoretical base for the proposed methodology with analytical expressions. The importance of inherent noise in the system and the behavior of resonant frequencies under various conditions are analyzed theoretically using mathematical computations. The validity of this methodology is then evaluated through a series of computer simulations run in MATLAB/Simulink. It is found that the results obtained from simulation closely match the theoretical analysis thus verifying the credibility of this methodology.

Next, the behavior of resonant frequencies is studied for a single line to ground fault case. Since resonant frequencies are unique to each system, every fault position along the cable length is uniquely represented by a set of resonant frequencies. It is this characteristic of resonant frequencies that helps in accurate estimation of fault location. A

detailed analysis of resonant frequency behavior under faulted conditions is carried out and the accuracy of fault estimation is determined.

Finally, the simulated results are compared with actual power system data. An appropriate choice of a window function and number of data points to be analyzed per block are made and the PSDs of the actual system voltage and current signal are obtained. Due to the presence of distortions in the current signal, further analysis on the current signal is not carried out. The comparison of simulated and actual system data shows a very close resemblance in terms of the resonant peak frequencies.

6.1 Key Aspects and Summary of Results

- → The resonant frequencies are observed in the power spectrum of the output signal only in the presence of inherent noise in the system (Section 3.4.1, Fig. 1).
- → The fundamental frequency for the transmission line only case, i.e., 'Case a', is found to be 3810 Hz (theoretical). For the simulated case, the fundamental frequency is found to be 3760 Hz which matches the theoretical value.
- → Based on theoretical computations, the fundamental frequency for the transformer case, i.e., 'Case b', is found to be 7620 Hz, twice that of 'Case a'. The fundamental frequency for the simulated 'Case b' is found to be 7665 Hz.
- → The output voltage spectra for 'Case b' shows no distinct resonant peaks when analyzed without a window function. However, the use of the Hann window overcomes this effect (Section 4.1.2, Fig. 4.7).
- → Under single line to ground fault conditions, every fault position is uniquely represented by a set of resonant frequencies when simulated with a fault resistance (R_F) value between 1 mΩ – 30 Ω (Section 4.2.1, Fig. 4.11).

→ For the case of a fault at the 50% point (for R_F between 1 mΩ – 30 Ω), it is observed that the fundamental frequency for the faulted and fault-free case are identical (Section 4.3, Fig. 4.17). Thus, a fault occurring at the 50% point should be identified by observing higher order, i.e., second and third order frequencies.

→ For fault resistance values greater than 30 Ω (Figs. 4.13 and 4.14), the resonant frequencies gradually begin to represent the fault-free power spectrum (Fig. 4.6).

→ The accuracy of this methodology in terms of fault location is found to be as high as locating a fault within a ±6.7 m range.

→ The THD of the actual voltage and current signal is found to be 1.24 % and 4.83 %, respectively, and fall within the prescribed IEEE standard.

→ The inherent noise level in the actual power system voltage and current signals is 0.0765 % and 0.4751 %, respectively.

→ Comparison of simulated data and analytical data with the actual system data shows a very close resemblance among all three data sets in terms of the resonant peak frequencies (Section 5.4, Fig. 5.7).

→ This work has resulted in the publication of a conference paper [41].

Based on the key aspects and results discussed above, it can be said that the proposed methodology is simple in terms of implementation and accurately estimates the location of cable faults which makes it a good option for real time testing and deployment.

Future work can include comparison of simulated fault data with actual system fault data, if available, to further validate this methodology. Also, a real time test environment implementing this methodology can be set-up in order to carry out practical testing.

REFERENCES

[1] A. A. Khan , N. Malik, A. Al-Arainy and S. Alghuwainem, "A Review of Condition Monitoring of Underground Power Cables," in *International Conference on Condition Monitoring and Diagnosis (CMD)*, Bali, 2012.

[2] CIGRE Working Group D1, "Knowledge Rules for Partial Discharge Diagnosis in Service," in *Cigre Technical Borchure*, Paris, CIGRE, 2003.

[3] J. C. H. Mejía, Characterization of Real Power Cable Defects by Diagnostic Measurements, Ph.D. Dissertation, Georgia Institute of Technology, Atlanta, 2008.

[4] Y. D. Kim, New Passive Methodology for Power Cable Monitoring and Fault Location, Ph.D. Dissertation, Arizona State University, Tempe, 2015.

[5] K. Butler-Purry and J. Cardoso, "Characterization of Underground Cable Incipient Behavior using Time-Frequency Multi-Resolution Analysis and Artificial Neural Networks," in *Power and Energy Society General Meeting*, Pennsylvania, 2008.

[6] Swift, G.W., "The Spectra of Fault-Induced Transients," *IEEE Transactions on Power Apparatus and Systems,* Vols. PAS-98, no. 3, pp. 940-947, May 1979.

[7] L.-Y. Wu, Z.-Y. He and Q.-Q. Qian, "A New Single Ended Fault Location Technique using Travelling Wave Natural Frequencies," in *Asia Pacific Power and Energy Engineering Conference*, Wuhan, China, 2009.

[8] Z. Haifeng, Q. Yulin and J. Huibin, "Medium voltage distribution network traveling wave fault location method based on wavelet packet energy spectrum," in *International Conference on Advanced Power System Automation and Protection (APAP)*, Beijing, China, 2011.

[9] T. Sidhu and Z. Xu, "Detection of incipient faults in distribution underground cables," *IEEE Transactions on Power Delivery*, vol. 25, no. 3, pp. 1363-1371, July 2010.

[10] W. Charytoniuk, "Arcing fault detection in underground distribution networks-feasibility study," *IEEE Transactions on Industry Applications,* vol. 36, no. 6, pp. 1756-1761, Dec 2000.

[11] M. M. Saha, J. J. Izykowski and E. Rosolowski, Fault Location on Power Networks, London: Springer, Oct. 2009.

[12] Emerson Network Power, "Partial Discharge Testing," Emerson, Columbus, OH., 2015.

[13] IEEE, Guide for Field Testing and Evaluation of the Insulation of Shielded Power Cable Systems, IEEE Std. 400-2001, April 2002.

[14] M. S. Mashikian and A. Szatkowski, "Medium Voltage Cable Defects Revealed," *IEEE Electrical Insulation Magazine,* vol. 22, no. 4, pp. 24-32, July 2006.

[15] HV Technologies, Inc., "Time Domain Reflectometer / TDR," HV Technologies, Inc., Manassas, VA, 2013.

[16] Megger, "A Guide To Diagnostic Insulation Testing Above 1 kV," Dallas, TX, 2010.

[17] Agilent Technologies, "Time Domain Reflectometry Theory," Agilent Technologies, Inc., 2013.

[18] Q. Shi, U. Troeltzsch and O. Kanoun, "Detection and Localization of Cable Faults by Time and Frequency Domain," in *7th International Multi-Conference on Systems, Signals and Devices*, Amman, 2010.

[19] G. Xu, Y. Zhou and Y. Chen, "Model-Based Fault Location with Frequency Domain for Power Traction System," *Energies,* vol. 6, no. 7, pp. 3097-3114, 2013.

[20] K. Zimmerman and D. Costello, "Impedance based fault location experience," in *58th Annual Conference for Protective Relay Engineers*, College Station, TX, 2005.

[21] Power System Relaying Committee of the IEEE Power Engineering Society, C37.114/D9-IEEE Guide for Determining Fault Location on AC Transmission and Distribution Lines, IEEE, 2005.

[22] P. Gale, P. Crossley, X. Bingyin, Y. Ge, B. Cory and J. Barker, "Fault location based on travelling waves," in *Fifth International Conference on Developments in Power System Protection*, York, 1993.

[23] C. Jensen, Online Location of Faults on AC Cables in Underground Transmission Systems, Springer, 2014.

[24] Z. Chen and J. Maun, "Artificial neural network approach to single ended fault locator for transmission lines," *IEEE Transactions on Power Systems*, vol. 15, no. 1, pp. 370-375, 2000.

[25] G. G. Karady and K. E. Holbert, Electrical Energy Conversion and Transport, Hoboken, New Jersey: John Wiley & Sons, Inc., 2013.

[26] BICC Cables, Electric Cables Handbook, Oxford, UK: Blackwell Science Ltd., 1997.

[27] N. Tleis, Power Systems Modelling and Faults Analysis:Theory and Practice, Boston, MA: Newnes, 2007.

[28] O. Coufal, "Inductance of Coaxial Cables," *Energy Spectrum,* pp. 1-5, January 2005.

[29] I. MathWorks, "power_cableparam," in *MATLAB R2015 Manual*, MathWorks, Inc., 2015.

[30] H. Eiichi, Applied ATP-EMTP to Highly-sophisticated Electric Power Systems, Tokyo: Tokyou Institute of Technology and Kyushu Institute of Technology, August 2003.

[31] J. D. Glover, M. S. Sarma and T. J. Overbye, "Transmission Lines: Steady State Operation," in *Power System Analysis and Design*, Stamford, CT, Cengage Learning, 2012, p. 254–262.

[32] K. Lin and K. E. Holbert, "Applying the equivalent pi circuit to the modeling of hydraulic pressurized lines," *Mathematics and Computers in Simulation,* vol. 79, no. 7, p. 2064–2075, March 2009.

[33] MathWorks, Inc., "Periodogram," in *MATLAB R2015b Documentation*, MathWorks.

[34] National Instruments, "Understanding FFTs and Windowing," 4 May 2015.

[35] P. Wickramarachi, "Effects of Windowing on the Spectral Content of a Signal," *Sound and Vibration,* vol. 37, no. 1, pp. 10-11, January 2003.

[36] IEEE Power and Energy Society, "IEEE Std. 519-2014 - IEEE Recommended Practice and Requirements for Harmonic Control in Electric Power Systems," IEEE, New York, NY, 2014.

[37] R. G. Wandhare and V. Agrawal, "A novel technique for thd control in grid connected photovoltaic systems using step variable inductor approach," in *35th IEEE Photovoltaic Specialists Conference (PVSC)*, Honolulu, HI, 2010.

[38] Mathworks, Inc., "Total harmonic distortion (thd)," in *MATLAB R2015b documentation*, Mathworks.

[39] Mathworks, Inc., "bandpower," in *MATLAB R2015b Documentation*, Mathworks.

[40] W. Rose, "Windowing, Part of HESC686-Mathematics and Signal Processing for Biomechanics," University of Delaware, Newark, 2011.

[41] S. Govindarajan, Y.-D. Kim and K. E. Holbert, "A Novel Methodology for Power Cable Monitoring using Frequency Domain Analysis," in *47th North American Power Symposium (NAPS)*, Charlotte, NC, 2015.

APPENDIX A

CABLE PARAMETER CALCULATION

1. Resistance

The resistance of underground cables is expressed as [26]

$$R_x = R_{AC} = R_{DC}\left[1 + y\left(k_s + k_p\right)\right] \ [\Omega/\text{km}\ ]$$

Where,

R_{AC} : equivalent AC circuit resistance (Ω/km)

R_{DC} : equivalent DC circuit resistance (Ω/km)

k_s : skin effect factor, k_s= 0.06678

k_p : proximity effect factor, k_p= 0.001125

y : constant which is equal to 1 in this case

$$R_{DC} = \frac{1.02 \times 10^6 \times \rho_{20}}{S}\ [1 + \alpha_{20}(\theta - 20)]$$

Where,

ρ_{20} : resistivity of the conductor material at 20^{o}C

For copper conductors, ρ_{20} = 1.7241 x 10^{-8} Ω.m

S : cross-sectional area of the conductor (mm^2), S = 1200 mm^2

α_{20} : temperature coefficient of the conductor material per K at 20^{o}C.

For copper conductors, α_{20} = 3.93 x 10^{-3} / K

θ : conductor operating temperature (^{o}C), θ = 75 ^{o}C

Substituting the values in the above equation

$$R_{DC} = \frac{1.02 \times 10^6 \times 1.7241 \text{ x } 10^{-8}}{1200}\ [1 + 3.93 \text{ x } 10^{-3}(75 - 20)]$$

$$R_{DC} = 1.7822 \text{ x } 10^{-5}\ \Omega.\text{m}$$

Now,

$$R_{AC} = R_{DC}\left[1 + y\left(k_s + k_p\right)\right]$$

$$R_{AC} = 1.7822 \text{ x } 10^{-5}[1 + 0.06678 + 0.001125]$$

$$R_{AC} = 0.019\ \Omega/\text{km}$$

2. Inductance

The inductance of underground cables is calculated as [28]

$$L_x = \frac{\mu_0}{2\pi} ln\left(\frac{r_o}{r_i}\right) \ [\mu H/km]$$

Where,

r_o : outer radius of the phase screen insulator, r_o = 0.03854 m

r_i : outer radius of the phase conductor including the conductor shield, r_i = 0.02154 m

μ_0 : permeability of free space, $\mu_0 = 4\pi \times 10^{-7}$ m.kg/s^2.A^2

$$L_x = \frac{4\pi \times 10^{-7}}{2\pi} ln\left(\frac{0.0384}{0.02154}\right)$$

$$L_x = 0.1156\ \text{mH/km}$$

3. Capacitance

The capacitance is calculated as [29]

$$C_x = 0.024 \frac{\varepsilon_r}{log\left(\frac{D}{d}\right)} \quad [\mu F/km]$$

Where,

D - outer diameter of the phase screen insulator, D = 0.03854 m

d - inner diameter of the phase screen insulator, d = 0.01954 m

ε_r - relative permittivity of insulation between sheath and earth, $\varepsilon_r = 4.1$

$$C_x = 0.02416 \frac{4.1}{log\left(\frac{0.03854}{0.01954}\right)} \ [nF/km]$$

$$\text{C}_\text{x} = 335.6\ \text{nF/km}$$

APPENDIX B

CABLE GEOMETRY

1. Cable Construction:

Copper Conductor/ XLPE Insulator/ Aluminum Sheath/ PVC (or PE) Sheath

Conductor Nominal Area (mm^2) / Shape	Approx. Thickness of Conductor Shield (mm)	Thickness of Insulation (mm)	Approx. Thickness of Insulation Shield (mm)	Thickness of Sheath (mm)	Thickness of Jacket (mm)	Overall Diameter (mm)
1200/SEG	2	17	1.3	2.6	4.5	127

SEG – Segmental Compacted

2. Cable Geometry:

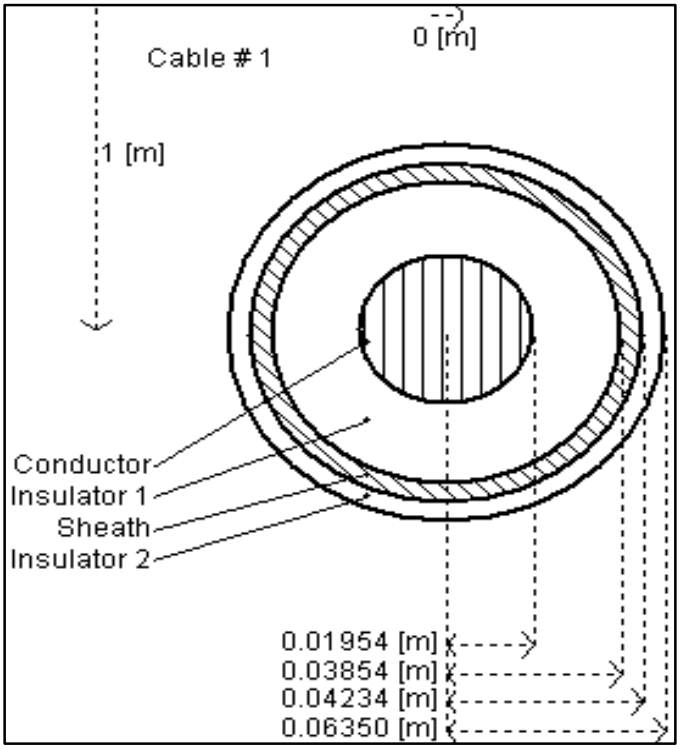

Fig. B.1 Cable Geometry